Effect of oscillator strength and intermediate resonance on the performance of resonant phonon-based terahertz quantum cascade lasers

S. Fathololoumi,[1,2] E. Dupont,[1,a)] Z. R. Wasilewski,[1,2] C. W. I. Chan,[3] S. G. Razavipour,[2] S. R. Laframboise,[1] Shengxi Huang,[3] Q. Hu,[3] D. Ban,[2,b)] and H. C. Liu[4]
[1]*National Research Council, Ottawa, Ontario K1A0R6, Canada*
[2]*Department of Electrical and Computer Engineering, Waterloo Institute for Nanotechnology, University of Waterloo, 200 University Ave W., Waterloo, Ontario N2L3G1, Canada*
[3]*Department of Electrical Engineering and Computer Science, Research Laboratory of Electronics, Massachusetts Institute of Technology, Cambridge, Massachusetts 02139, USA*
[4]*Key Laboratory of Artificial Structures and Quantum Control, Department of Physics, Shanghai Jiao Tong University, Shanghai 200240, China*

(Received 16 January 2013; accepted 4 March 2013; published online 20 March 2013)

We experimentally investigated the effect of oscillator strength (radiative transition diagonality) on the performance of resonant phonon-based terahertz quantum cascade lasers that have been optimized using a simplified density matrix formalism. Our results show that the maximum lasing temperature (T_{max}) is roughly independent of laser transition diagonality within the lasing frequency range of the devices under test (3.2–3.7 THz) when cavity loss is kept low. Furthermore, the threshold current can be lowered by employing more diagonal transition designs, which can effectively suppress parasitic leakage caused by intermediate resonance between the injection and the downstream extraction levels. Nevertheless, the current carrying capacity through the designed lasing channel in more diagonal designs may sacrifice even more, leading to electrical instability and, potentially, complete inhibition of the device's lasing operation. We propose a hypothesis based on electric-field domain formation and competition/switching of different current-carrying channels to explain observed electrical instability in devices with lower oscillator strengths. The study indicates that not only should designers maximize T_{max} during device optimization but also they should always consider the risk of electrical instability in device operation. © *2013 American Institute of Physics*. [http://dx.doi.org/10.1063/1.4795614]

I. INTRODUCTION

Since terahertz (THz) quantum cascade lasers (QCLs) were first demonstrated in 2002,[1] device temperature performance has remained a hot topic for the THz QCL research community.[2] This research area has been driven by scientific curiosity, exploring whether the maximum operating temperature (T_{max}) can exceed the empirical limit of $T_{max} < \hbar\omega/k_B$ in resonant tunneling quantum cascade lasers (RT-QCL), which was qualitatively explained in Ref. 3, and, more importantly, by increasing demands for compact, solid-state based and coherent terahertz sources with average optical power levels far greater than one milliwatt. In particular, THz QCLs designed to operate effectively within thermoelectric cooler temperatures or, better yet, up to room temperature will open up a broad range of opportunities for new THz applications in many important areas, including high speed communications, pharmacology, non-invasive cross sectional imaging, gas and pollution sensing, heterodyne detection, and security screening.[4–6] Although researchers have continued to improve device performance by designing new lasing schemes with higher optical gain,[7–14] optimizing injection/extraction barrier thickness,[15,16] characterizing doping concentration effects,[17–19] and reducing waveguide losses,[20–22] THz QCLs have yet to achieve room-temperature operation. To date, resonant phonon-based THz QCLs demonstrate the strongest potential to realize this level of performance.[9,10,23]

Several theoretical models have been employed to understand the details of charge transport and optical gain within THz QCLs, including density matrix (DM) formalism,[24–26] the non-equilibrium Green's function,[27–29] and Monte Carlo (MC) techniques.[30–34] For example, using a simplified density matrix (SDM) model, it has been found that the population inversion of three-well resonant phonon-based active regions is lowered because of existing parasitic injection and extraction tunneling channels.[25,26] Kumar *et al.* proposed a more diagonal lasing transition design to increase the upper lasing state (ULS) lifetime and reduce the strength of undesired tunnel couplings (parasitic leakages), which leads to an improved population inversion at higher temperatures and a T_{max} of 186 K at 3.9 THz.[10] Further optimization of oscillator strength and injection tunneling has been shown to improve device performance, with THz QCLs recently achieving operating temperatures up to 199.5 K in the absence of a magnetic field.[23]

The intersubband gain (g_{isb}) of a THz QCL depends on the product of population inversion ($\Delta\rho$) and oscillator strength $f_{ul} = (2m^*\omega_{ul}z_{ul}^2)/\hbar$ ($g_{isb} \propto f_{ul} \times \Delta\rho$); thus, although lower oscillator strengths are expected to suppress parasitic leakage, they are also expected to reduce the intersubband

a)emmanuel.dupont@nrc.ca
b)dban@uwaterloo.ca

gains. Mátyás *et al*. used a MC approach to theoretically study the temperature dependence of population inversion, spectral bandwidth, and optical gain across several degrees of diagonality and laser frequencies.[33] Their MC simulations showed that for frequencies above ~3.5 THz, the increased diagonality of the lasing transition is beneficial between 150 and 200 K. However, below ~3.5 THz, increasing diagonality only marginally improves population inversion at higher temperatures and hence does not fully compensate for the impacts of low oscillator strength. Belkin *et al*.[35] experimentally compared vertical and diagonal transition structures at a lasing frequency of ~3.15 THz and demonstrated that both devices exhibit similar T_{max}. More recently, Chassagneux *et al*. studied a series of vertical designs tuned at different frequencies (2.3–3.8 THz) with similar injection (1 meV) and extraction (2 meV) coupling strengths. They pointed out that resonant phonon-based THz QCL performance is limited by the interplay between two factors: (i) optical phonon scattering of thermal electrons (dominant at higher frequencies) and (ii) parasitic leakage current (dominant at lower frequencies).[36] In particular, parasitic leakage was largely attributed to the coupling (which will be called intermediate resonance in this paper) between the injection and the immediate downstream extraction levels, which typically occurs shortly before the lasing threshold point. Although theoretical models have successfully been developed to satisfactorily explain many experimental observations,[37] discrepancies continue to emerge between experimental and simulation results when these models are applied to design new structures with improved performance.[38] In many cases, experiments are still the ultimate approach to verify hypotheses.

In this paper we report the results of a systematic study aimed at characterizing the effects of oscillator strength and intermediate resonance on resonant phonon-based THz QCL performance. Our combined experimental and theoretical approach reveals that the effect of oscillator strength on T_{max} may be more complicated than previously thought. Depending on the optical loss of the laser waveguide, oscillator strength in DM-optimized QCLs may be one of the key optimization parameters in seeking the highest T_{max} when optical loss is high or may play an insignificant role in this effort when optical loss is low. This study also confirms an earlier hypothesis presented in Ref. 3, namely, that great care should be taken to limit intermediate resonance in RT-QCL designs to ensure the associated parasitic leakage current does not become dominant in lasers with low oscillator strengths and/or that are operated in low temperatures. Competition between the intermediate resonance leakage channel and the designed lasing channel is manifested in devices with various oscillator strengths, leading to electrical and optical instability in device operation.

The paper is organized as follows. In Sec. II, we describe how our SDM-based approach was applied to optimize QCL devices that emit ~15 meV photon energy and present five resulting designs with different degrees of laser transition diagonality. In Sec. III, we report experimental results illustrating Au double metal ridge laser device performance at different temperatures. In Sec. IV, the five designs are analyzed across three performance characteristics, namely, (a) maximum operating temperature, which confirms its weak dependence on laser transition diagonality due to the low waveguide loss in our devices, (b) leakage current prior to threshold due to tunneling resonance between two successive phonon wells, which can be modeled using our SDM technique and minimized by carefully tuning the injection and extraction resonances, and (c) electrical characteristic instability, observed in highly diagonal structures, which are interpreted with a qualitative model based on the formation of electric field domains. Finally, Sec. V summarizes our conclusions. An appendix shows the high temperature performance of a highly diagonal RT-QCL structure processed with a copper double metal waveguide.

II. MODELLING, EPITAXIAL GROWTH, AND DEVICE FABRICATION

The design process began with finding a series of lasing double-wells with intersubband resonance at 15 meV, all based on the GaAs/$Al_{0.15}Ga_{0.85}As$ material system. Seven different oscillator strengths within the lasing double-well were selected, $f_{ul} \approx 0.20$, 0.26, 0.30, 0.35, 0.41, 0.47, and 0.66 at a design electric field ~12 kV/cm. Note that these values were calculated from an isolated double-well without coupling to the adjacent quantum wells. Initially we assumed the lasing double-well (with 3: the lower and 2: the upper lasing states) is isolated from the upstream and downstream phonon wells. Both phonon wells, shown in Figure 1, contain one injector (1) and one extractor (4) states. The injection and extraction barrier thicknesses play important roles in populating and depopulating the lasing levels,[15,16] as well as in defining the linewidth and amplitude of the gain.[26] We used the SDM approach to optimize the barrier thickness for each device design. Despite its rather simple and fast computation process, this SDM model provides essential design guidelines that include all the tunnel couplings and several intrawell intersubband scattering mechanisms (e-LO phonon, e-impurity, and interface roughness scatterings).[26]

For each of the designs, several phonon well thicknesses were considered during the optimization process. Table I shows the detailed simulation results for seven designs, each with different degree of diagonality. We thereafter refer the designs as f-series design and resulting device samples as f-series devices because they have different oscillator strength (f_{ul}). The optimization exercise converged towards rather thin injection and extraction barriers, and we found the pairs of states across these barriers (1-2 for injection and 3-4 for extraction) were aligned at about the same electric field (~12 kV/cm). The convergence of the model towards thinner barriers is mostly driven by the maximization of population inversion but is constrained by parasitic leakages (the wrong injection: 1 → 3 and the wrong extraction: 2 → 4 channels) and by the gain broadening that is induced by tunneling couplings (1-2 and 3-4). Simulation results presented in Table I show that the wrong extraction coupling strength (Ω_{24}) is more than three times as large as the wrong injection coupling strength (Ω_{13}) in all f-series designs, which indicates that the wrong injection leakage coupling channel (1-3) is less likely to be a source of concern than the wrong

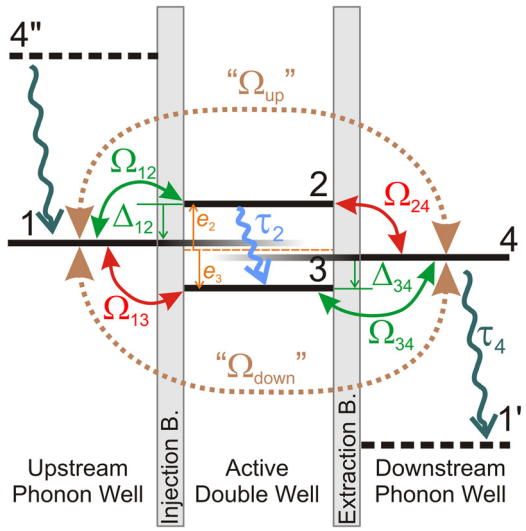

FIG. 1. A schematic diagram of the four relevant states in a three-well resonant phonon-based THz QCL. Ω_{ij} are the tunnel coupling strengths. The injection (Ω_{12}) and the extraction (Ω_{34}) coupling channels are shown in green, while undesired parasitic leakage channels such as the wrong injection (Ω_{13}) and wrong extraction (Ω_{24}) are shown in red. The detuning energies between states are noted $\Delta_{ij}=E_i$-E_j. The double side dashed arrow represents the indirect coupling between states 1 and 4 via the couplings $1 \leftrightarrow 2 \leftrightarrow 4$ and $1 \leftrightarrow 3 \leftrightarrow 4$, which cause a small anticrossing AX_{14} when states 1 and 4 are close to alignment. Explanations for the Ω_{up} and Ω_{down} "couplings" are given in Sec. IV B.

extraction leakage channel (2-4).[26] When the voltage drop per module corresponds to the LO-phonon energy, states 1 and 4 are aligned and can hybridize each other due to two chains of successive interactions which involve the wrong tunneling strengths: $1 \leftrightarrow 2 \leftrightarrow 4$ and $1 \leftrightarrow 3 \leftrightarrow 4$.

The gain spectrum linewidth is strongly influenced by the injection and extraction tunnelings, and it was determined in the same way as described in Refs. 23 and 26—pure dephasing time constants of tunneling ($\tau^*=0.35$ ps) and of optical intersubband transition ($\tau_{23}^* \sim 1.1$ ps) were used in our SDM simulation. Longer τ^* would try to reveal the doublets on the injection and extraction sides, hence increasing the full width at half maximum of the gain spectrum.[25,26] To simplify the optimization process these pure dephasing times were chosen independent of temperature and diagonality. This hypothesis could be considered as an oversimplification;[39] for instance, more diagonal intersubband transitions—at least in the mid-infrared spectral range—tend to show broader resonances (shorter τ_{23}^*). Each of the designs was optimized independently of the laser threshold current density in order to maximize the operating temperature at which the intersubband gain coefficient of $g_{isb}=35\,cm^{-1}$ can be maintained. Therefore, we did not expect the phonon well and the injection and extraction barrier thicknesses to remain exactly constant among the seven f-series designs. As a result, in addition to the oscillator strength, the tunnel coupling strengths also differ among the seven designs. Interestingly, Table I shows a general trend of decreased tunnel coupling strength as diagonality increases. As tunnel coupling strengths (Ω_{12} and Ω_{34}) decrease, it takes longer for electrons to tunnel through the injection and extraction barriers. As diagonality increases (f_{ul} gets smaller), the carrier lifetime at the upper lasing state (τ_2) becomes longer; therefore, longer injection and extraction tunneling times is more tolerable because the same population inversion could still be sustained for lasing operation. Reduced tunnel coupling strengths, on the other hand, offer different benefits; that is, by suppressing the broadening of the gain spectrum, a higher peak gain may be achieved. This explains why the design optimization, which targets maximized peak gain, converged

TABLE I. Simulation parameters and results of seven designs that were optimized using a SDM formalism approach. The experimental results are summarized in the last four rows; with a subscript "exp Au" the numbers are relative to Au-Au double metal ridge waveguides, ~1 mm long and ~143-144 μm wide, and with a subscript "exp Cu" to Cu-Cu waveguides fabricated at MIT."

Oscillator strength (f_{23}) (grown wafer ID)	0.66	0.47 (V775)	0.41 (V813-14)	0.35 (V774)	0.30 (V812)	0.26 (V773)	0.20
τ_{23} ($E_k=E_{LO}$-E_{23}) (ps)	0.313	0.453	0.54	0.639	0.772	0.915	1.228
$f_{23} \times \tau_{23}$	0.207	0.215	0.220	0.226	0.232	0.237	0.243
Ω_{12} (meV)	1.356	1.378	1.344	1.315	1.287	1.231	0.998
Ω_{34} (meV)	2.698	2.468	2.33	2.3	2.18	2.021	1.689
Ω_{13} (meV)	−0.728	−0.474	−0.4	−0.345	−0.295	−0.253	−0.172
Ω_{24} (meV)	2.903	1.724	1.42	1.246	1.043	0.872	0.613
F_{AX} (kV/cm)	8.58	8.84	8.76	8.81	8.82	8.7	8.52
AX_{14} (meV)	1.2903	0.973	0.837	0.747	0.637	0.536	0.3287
Ω_{up} (meV)	1.97	1.572	1.42	1.323	1.204	1.081	0.822
Ω_{down} (meV)	1.407	1.155	1.05	0.98	0.895	0.806	0.616
$r=\Omega_{down}/\Omega_{up}$	0.714	0.735	0.74	0.741	0.743	0.746	0.749
Injection barrier (nm)	40	43	44	45	46	47	52
Left lasing well (nm)	96.5	89	88	87	86	86	85
Radiative barrier (nm)	19.3	24.6	27	29.1	31.7	33.9	38.3
Right lasing well (nm)	77	81.5	82.5	83	83	83.5	83
Extraction barrier (nm)	35	41	43	44	46	48	53
Phonon well (nm)	163	160	160	159	158	158	157
$J_{th,exp\ Au}$ (10 K) (A/cm^2)	···	973	934	662	658	510	···
$J_{max,exp\ Au}$ (10 K) (A/cm^2)	···	1461	1483	939	1003	807	···
$T_{max,exp\ Au}$ (K)	···	180	176.5	169	160	162.5	···
$T_{max,exp\ Cu}$ (K)	···	199.5	187	197	199.3	184	···

to a gradual decline of the tunnel coupling strengths as oscillator strength decreased. Note that the product between oscillator strength (f_{23}) and upper lasing state lifetime (τ_{23}) by e-LO phonon scattering increases slowly with diagonality, as shown in Table I.

By ignoring the wrong injection and wrong extraction leakage channels ($\Omega_{24}=0$, $\Omega_{13}=0$), the population inversion between ULS and lower lasing state (LLS) can be estimated simply by[26]

$$\Delta\rho = \frac{\tau_2 - T_{34} - \tau_4}{2\tau_2 + T_{12} + T_{34} + 2\tau_4} \quad (1)$$

with

$$\frac{1}{\tau_2} \approx (1+n_{\mathrm{LO}})\tau^{-1}_{2,\mathrm{LO\,emi}}\Big|_{E_k=E_{\mathrm{LO}}-E_{23}} e^{-\frac{E_{\mathrm{LO}}-E_{23}}{kT_e}} + \frac{1}{\tau_2}\Big|_{T_e=0}, \quad (2)$$

where τ_2 and τ_4 are the carrier lifetimes for the upper lasing (2) and extraction (4) levels, respectively, T_{12} and T_{34} are the tunneling times for 1-2 and 3-4 resonances, respectively, n_{LO} is the occupation number of LO phonons, E_{LO} is the LO phonon energy, E_{23} is the radiative transition energy (lasing photon energy), and T_e is the hot electron temperature. In this simple calculation—and actually through all SDM simulations of this work—the hot electron temperature was assumed to be 90 K higher than the lattice temperature,[40] and a zero temperature lifetime of 10 ps ($\tau_2|_{T_e=0}$) was inferred. These two equations show that in order to make the population inversion as weakly dependent as possible on the thermally activated exponential of the $2 \rightarrow 3$ scattering rate, the resonant intersubband lifetime (the prefactor $\tau_{2,\mathrm{LO\,emi}}|_{E_k=E_{\mathrm{LO}}-E_{23}}$) should be kept as long as possible. Thus, diagonal lasing transitions should be preferred to maintain high population inversion at elevated temperatures.

Figure 2 shows the product of calculated population inversion and oscillator strength ($\Delta\rho \times f_{23}$) versus temperature for the seven designs shown in Table I. Since the intersubband gain is proportional to this product, one can see that the optical gain drops with temperature in all of the seven designs. At low temperatures (below 50 K), the gain for very diagonal designs suffers due to the small oscillator strength (f_{23}). As temperature increases, the curves of less diagonal designs drop faster than those of more diagonal designs. The designs with medium-range diagonality ($f_{23}=0.47$-0.41) appear to exhibit the best performance at temperatures below 140 K. Around 145 K, designs with $f_{23}=0.47$-0.35 may have similar performance. At ~165 K, designs with $f_{23}=0.41$-0.35 may perform equally, and at ~187 K it is not clear which design within the range of $f_{23}=0.41$-0.30 performs the best. Therefore, the back-of-the-envelope calculation performed using Eq. (1) did not convincingly reveal an optimum oscillator strength, similar to the MC optimization results in Ref. 33. In Sec. IV, we will see that the SDM simulation results suggest that a $T_{\max}$ of ~170 K could be achieved for all of the seven SDM-optimized designs given that the threshold gain remains constant at 25 cm^{-1}. Hence it is necessary to determine the optimum oscillator strength experimentally.

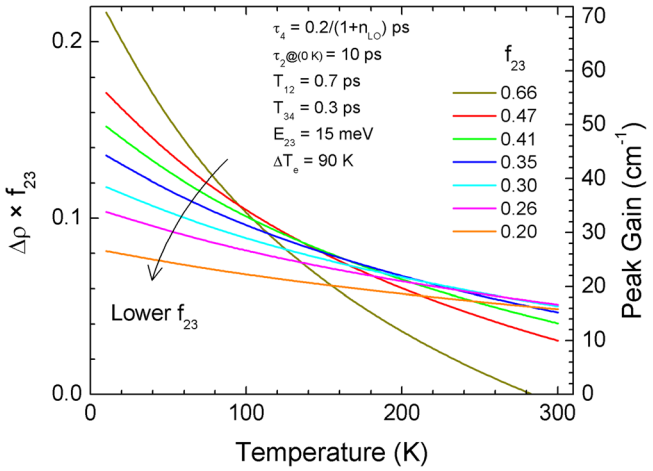

FIG. 2. Product of population inversion and oscillator strength ($\Delta\rho \times f_{23}$) versus temperature for the seven designs presented in Table I. The curves were obtained from Eqs. (1) and (2), the radiative transition, E_{23}, was set to 15 meV, the hot electron temperature was set 90 K higher than the lattice temperature, and a 10 ps temperature independent lifetime component was assumed. The right scale translates the product $\Delta\rho \times f_{23}$ into a coarse estimation of peak gain by assuming a 3D carrier concentration of $7 \times 10^{15}\,\mathrm{cm}^{-3}$ and a gain spectrum bandwidth of ~1.5 THz.

We used molecular beam epitaxy technique to separately grow five out of the seven optimized designs ($f_{\mathrm{ul}} \approx 0.26$, 0.30, 0.35, 0.41, and 0.47) on semi-insulating GaAs substrates. The number of quantum cascade modules in each growth, N, was produced corresponding to a 10 μm thick active region. A sheet electron density of $n_s = 3 \times 10^{10}\,\mathrm{cm}^{-2}$ per period was achieved using uniform Si-doping within the middle 5 nm of the phonon well. The active region was sandwiched between a bottom layer comprising 100 nm of $5 \times 10^{18}\,\mathrm{cm}^{-3}$ n^+ GaAs and a top stack of 50 nm of $5 \times 10^{18}\,\mathrm{cm}^{-3}$ n-doped, 10 nm of $4 \times 10^{19}\,\mathrm{cm}^{-3}$ n^+-doped and 3.5 nm of low-temperature grown GaAs layers. Special emphasis was put on minimizing the drift of Ga and Al fluxes during this long growth process. The X-ray diffraction rocking curve could be perfectly fitted with nominal parameters, with no extra broadening of satellites peaks, confirming the excellent stability of the growth rates (better than 0.5%) throughout the active region. The wafers were then processed into THz QCL devices with Au double metal waveguides. The five fabricated devices (which will be called f-series devices in this paper) have the following dimensions: ~143–144 μm wide ridges with ~130 μm (for wafers V775, V814, V773) or ~120 μm (for wafers V774, V812) wide top Ti/Au metallization forming a Schottky contact, and ~1 mm long Fabry-Pérot resonator. An In-Au wafer bonding technique was used,[20] and waveguide ridges were fabricated using reactive-ion etching. Other device fabrication details can be found in Ref. 22. We are aware that different widths of exposed top contact layer between the Schottky contact and the edge of the ridge may introduce small variations in waveguide loss.

III. EXPERIMENTAL RESULTS

Temperature-dependent pulsed L-J (light-current density) curves corresponding to the f-series THz QCL devices, each with a different oscillator strength (f_{ul}) ranging from 0.26 to 0.47 (denoted f26–f47), are plotted in Figure 3.

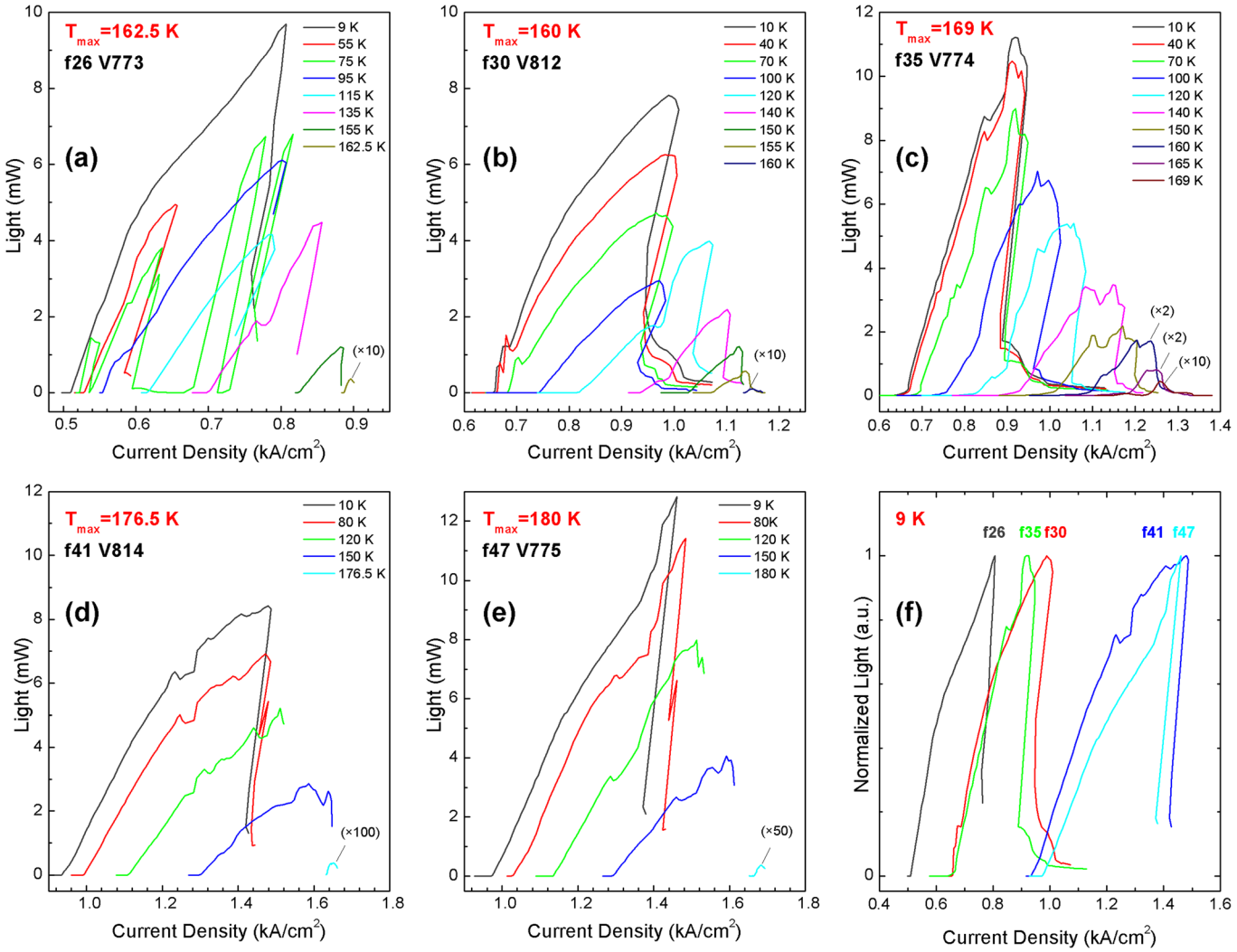

FIG. 3. Pulsed L-J curves of the f-series devices at different temperatures. (a)–(e) f26, f30, f35, f41, and f47, respectively. (f) Normalized light vs. current density at 10 K for the five f-series devices with similar dimensions of ~144 um wide waveguide and ~1 mm long cavity length.

The devices were biased in pulsed mode with pulse width of 250 ns and repetition rate of 1 kHz. All five devices lased above 160 K; however, the device with $f_{ul} = 0.475$ achieved the highest T_{max} at 180 K, which was reported in Ref. 23. The peak emission power of all five devices reached a minimum of 8 mW, with some achieving higher values at ~10 K. The threshold current density ranges from ~0.51 kA/cm^2 to ~1.67 kA/cm^2, depending on the operating temperature and QCL design under test. Figure 3(f) shows a general trend that the threshold current density increases as oscillator strength increases from 0.26 to 0.47. This is attributed to higher leakage current in more vertical designs. The leakage current is related to the parasitic channel of the intermediate resonance (1-4) and the wrong extraction channel (2-4), which will be discussed in more detail in Sec. IV.

Lasing spectra of the f-series devices are plotted in Figure 4. At 10 K, all five devices exhibit multiple Fabry-Pérot (FP) modes. The lasing frequencies gradually shift from ~3.3 THz down to ~2.85 THz as the oscillator strength increases from 0.26 to 0.47. At higher temperatures that are close to their respective T_{max}, the lasing frequencies of the five devices blue shifted by 0.3–0.6 THz (10–20 cm^{-1}). This is due to the Stark effect as the threshold voltage increases with temperature and the energy separation between the upper and lower lasing states become larger at higher biases. The measured lasing frequency at high temperature, i.e., close to the design electric field, deviates from the design value $\Delta_{23}/\hbar \sim 3.65$ THz. The lasing frequency is sensitive to the photon driven current, which decreases the resistance of the lasing double wells and might lead to a non-uniform electric field above threshold.[41] Lasing frequency prediction is certainly not a trivial task.[23] In a single electron picture, a more complete calculation needs a self-consistent simulation that includes quantum carrier transport, stimulated emission, and the Schrödinger and Poisson equations must be solved simultaneously. Furthermore, solving this problem becomes even more complex when many-body effects are included.[42] The optical gain at temperatures close to T_{max} only narrowly beats the optical loss, and, as a result, fewer FP modes can sustain lasing operation. In particular, the f35 and f47 devices were able to continue lasing in single FP mode at 160 K and 165 K, respectively.

Figure 5(a) shows the threshold current density vs. temperature for the five devices from ~10 K up to their

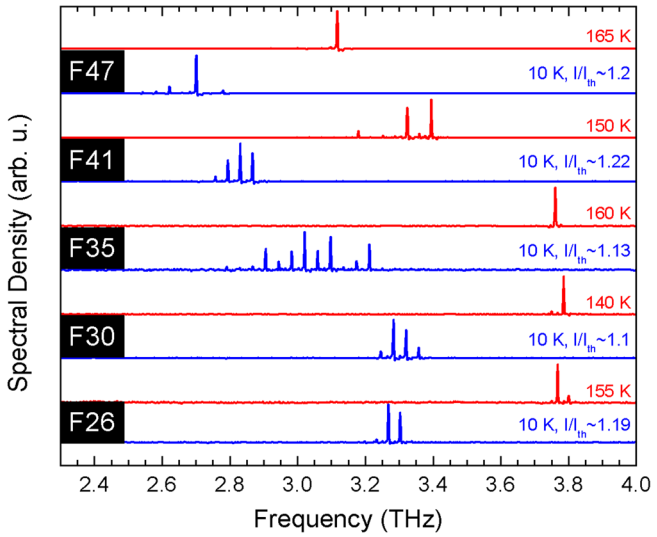

FIG. 4. Lasing spectra of the f-series structures (f26-f47) tested with Au double-metal ridge waveguides at 10 K and temperatures close to their respective T_{max}.

respective T_{max}. As expected, all J_{th} increase exponentially with temperature. At most of the temperatures, devices with lower oscillator strengths exhibit lower threshold current. All five devices show similar temperature dependence of threshold current density. The relative dynamic range (RDR), defined as $(J_{max} - J_{th})/J_{max}$, is plotted in Figure 5(b). At first sight, the RDR of the five structures show similar temperature dependences, with a low-temperature value (i.e., 10 K) confined in a narrow range of 0.3–0.37. However, a closer view reveals different behaviours between wafers, for instance f26 versus f35. The former has a higher RDR value at 10 K, but it drops quickly to zero as temperature increases, whereas the RDR of the latter is less sensitive to temperature up to 140 K even though its value at 10 K is smaller. This shows that there is not a clear-cut correlation between RDR at low temperature and T_{max}.

IV. DISCUSSIONS

A. Maximum lasing temperature (T_{max})

We will first examine the effect of oscillator strength on T_{max} achieved by our SDM optimized QCL structures. Numerical simulation was performed to calculate T_{max} as a function of oscillator strength under different cavity loss condition (20–35 cm^{-1}). Simulation modelling was based on the density matrix approach described in Ref. 26; however, with some modifications to enhance accuracy, for instance by including interface roughness scattering. The rotating wave approximation was not used in the simulation, meaning the off-resonant terms of coherence terms were taken into account.[43] The results are plotted in Figure 6. It is important to realize that the x-axis label of this figure ("Oscillator Strength") is not generic but rather corresponds directly to the specific oscillator strengths of the SDM optimized structures. As expected, across the range of relevant oscillator strengths, from 0.2 to 0.66, the theoretical T_{max} was significantly improved by reducing cavity loss. In fact, the calculated increase of the T_{max} with reduction of cavity loss is in

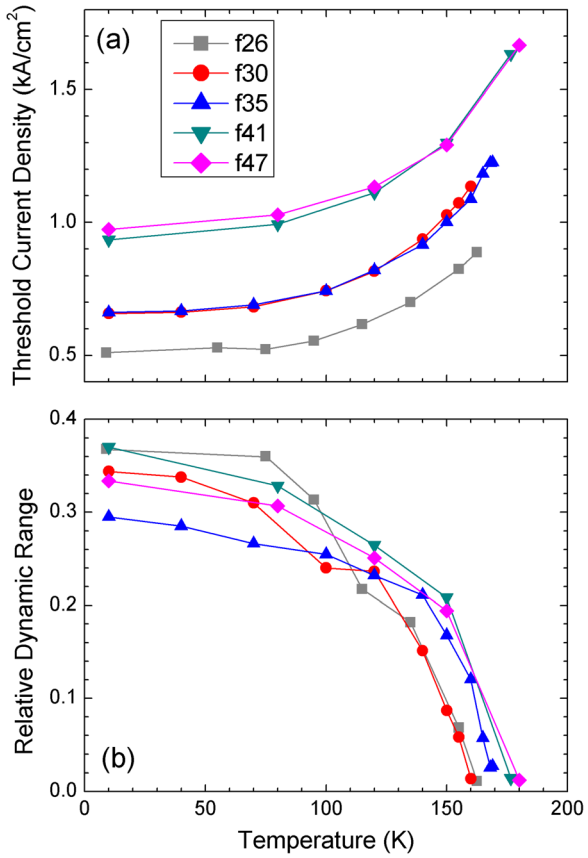

FIG. 5. (a) Threshold current density (J_{th}) vs. heat sink temperature for the f-series devices with Au-Au waveguides and different oscillator strengths. (b) Relative dynamic range vs. temperature for the same set of devices.

good agreement with a recent experiment which measured the peak gain decreases with temperature by ~1 cm^{-1} for a 10 K increase in temperature.[44] The figure also shows that depending on the level of cavity loss, oscillator strength in the SDM optimized structures can play different roles in determining T_{max}. For example, when the optical loss is 35 cm^{-1}, higher oscillator strengths ($f_{ul} = 0.44$-0.6) appear to be more advantageous, enabling higher T_{max}. In contrast, when optical loss is low (i.e., 20 cm^{-1}), structure with lower oscillator strengths, such as $f_{ul} = 0.3$, may demonstrate the best T_{max} performance. Our findings from Figure 6 are consistent with the simple calculation illustrated in Figure 2. When intermediate optical loss occurs (such as 25-30 cm^{-1}), it seems that the optimum oscillator strength is in the intermediate range (0.3-0.5), and more interestingly, T_{max} almost remains constant over a wide range of oscillator strengths, which means that oscillator strength may not be critical in optimizing T_{max} if the whole structure has been optimized at each given oscillator strength.

Experimental T_{max} data are also plotted in Figure 6 for comparison. As can be seen, the T_{max} of the f-series devices fabricated with a Au-Au metal waveguide structure fits reasonably well with the theoretical curves corresponding to a cavity loss of 29–30 cm^{-1}. The T_{max} of f26, f41, f47 devices is almost on the 29 cm^{-1} cavity loss curve, while the T_{max} of f30 and f35 devices agrees more with the 30 cm^{-1} cavity loss curve. This small discrepancy is attributed to small

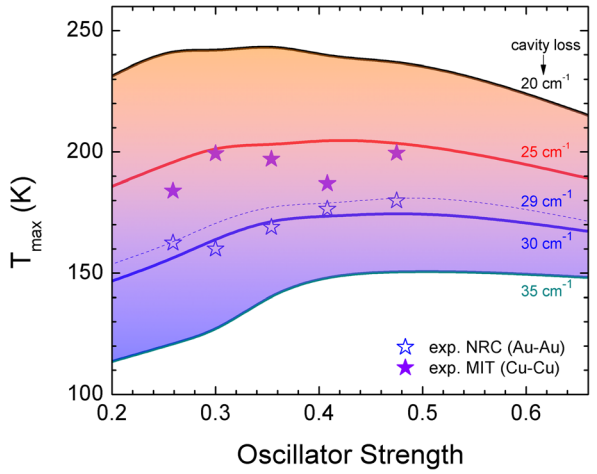

FIG. 6. Theoretical and experimental T_{max} vs. oscillator strength in SDM optimized QCL structures. The continuous lines are T_{max} values theoretically predicted using simplified density matrix formalism under different cavity losses (20, 25, 29, 30, 35 cm^{-1}). The open star symbols represent experimental T_{max} for f-series devices with Au-Au waveguides and the solid star symbols represent experimental T_{max} for f-series devices with Cu-Cu waveguides and the top n-GaAs contact layer removed.

waveguide loss fluctuation during the device fabrication process. The width of the top Ti/Au contact metal was targeted to be 130 μm in device fabrication; however, from optical and scanning electron microscope inspections conducted after device fabrication, it was found that the top metal width of the f26, f41, and f47 devices was 130 μm while that of the f30 and f35 was 120 μm. The narrower top Ti/Au layer slightly inflates the cavity loss and thus explains why the cavity loss observed for the f30 and f35 devices is $\sim$1 cm^{-1} higher than that of the other devices.

Removing the top n^+ GaAs contact layer and adopting a Cu-Cu waveguide can typically reduce cavity loss by 4-5 cm^{-1}.[9,23,37] One would expect these QCLs to demonstrate significantly improved T_{max}. The f26, f30, f35, f41, and f47 wafers were re-processed with a Cu-Cu waveguide, and their T_{max} were measured. As shown in Figure 6, the T_{max} achieved by all devices with Cu-Cu waveguides was indeed higher than devices equipped with Au-Au waveguides. In particular, re-processing the f30 device with a Cu-Cu waveguide enhanced its T_{max} from 160 K to 199.3 K and that of the f47 device showed similar improvement from 180 K to 199.5 K.[23] The appendix reports L-J characteristics of the f30 device with a Cu-Cu waveguide. The small 10.5 K difference in T_{max} for the two types of waveguide on V814 (f41) comes from major device damages during the fabrication.[45] With the exception of f41, the experimental data are in reasonable agreement with theoretical predictions corresponding to a cavity loss of 25 cm^{-1}.

As temperature increases, the upper lasing lifetime decreases and consequently the optical gain degrades. The degradation rate of the optical gain with temperature differs across designs with different oscillator strengths. The simulation results show that the gain degradation rate per unit temperature rise is slower for devices with lower oscillator strengths—the separation among the T_{max} curves corresponding to different cavity losses in Figure 6 becomes wider as the oscillator strength goes from 0.66 to 0.2. The experimental data support the simulation results—the f30 device's T_{max} rises by 39.3 K while the f47 T_{max} increases by 19.5 K for a similar reduction in cavity loss. This suggests that designs with lower oscillator strengths are more sensitive to cavity loss.

B. Threshold current density and 1-4 anticrossing (intermediate resonance)

Figure 3(f) shows the normalized light vs. current density at 10 K for the five f-series devices with Au-Au waveguides. As oscillator strength decreases, the threshold current density decreases and the dynamic range exhibits a diminishing trend (except f35 devices). The decrease in threshold current density can largely be attributed to the reduced leakage current associated with a more diagonal design.[36] Leakage current is mainly the result of the intermediate resonance that occurs between the injection level and the following downstream extraction level when they align at a bias slightly below the threshold point (Figure 7). In addition, the wrong extraction leakage current (2-4) also decreases with decreases in oscillator strength. As shown in Table I, Ω_{24} decreases from 1.724 meV to 0.872 meV as oscillator strength decreases from f47 to f26, indicating a strongly suppressed leakage current through the wrong extraction channel.

From f47 to f30, we observed a general trend towards a slow decrease in dynamic range (J_{max}-J_{th}) with diagonality, which can be *qualitatively* interpreted by using a three-level model[3,12,25,46] and by ignoring temporarily the anticrossing between levels 1 and 4. The increase in J_{max} with oscillator

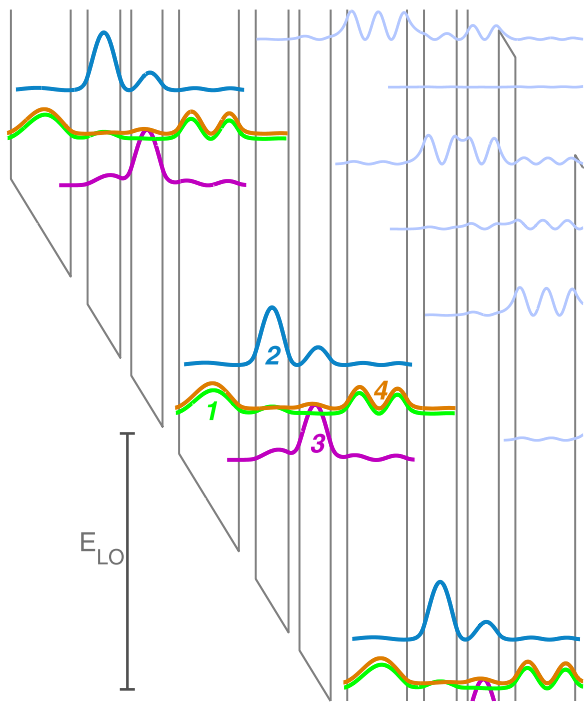

FIG. 7. Conduction band diagram of the f35 QCL active region at an electric field of 8.8 kV/cm, at which the injection level (1) aligns with extraction level (4), resulting in a $\sim$0.75 meV anticrossing energy (AX_{14}) between the hybridized states. This intermediate resonance between levels 1 and 4 creates a parasitic leakage channel, which can be dominant when the lasing oscillator strength is very low.

strength can be explained by (i) faster carrier transport through the wrong extraction channel ($2 \rightarrow 4 \rightarrow 1'$) and (ii) decreased population inversion at lasing threshold. Both factors contribute to decrease in the fractional change of differential resistance at threshold,[12] $(\Delta R_{ac}/R_{ac})|_{th}$, and the first factor decreases the transit time (in the stimulated emission regime) between two successive injection barriers, hence penalizes the coherence criteria of carrier transport above threshold, leading to additional increase in J_{max}. We recall that the maximum current is strongly related to the gain characteristics of the active region and the intra-cavity laser field intensity. With a simple rate equation model, this effect is summarized through the following equations:[12]

$$\begin{aligned} J_{max} &\propto \left(1 - (\Delta R_{ac}/R_{ac})|_{th}\right) \\ 1 - (\Delta R_{ac}/R_{ac})|_{th} &\approx 1 - 2\Delta\rho_{th}\eta \\ &\approx 1 - 2\eta\frac{\alpha_{cav}}{\Gamma\sigma N_{3D}}, \end{aligned} \tag{3}$$

where η is the internal quantum efficiency of laser emission (which should increase with diagonality), $\Delta\rho_{th}$ the normalized population inversion at threshold, α_{cav} the total cavity loss coefficient, σ the gain cross-section of the active region, Γ the laser field overlap with the active region, and N_{3D} is the three-dimensional carrier density in the active region. For this qualitative discussion on J_{max} vs. oscillator strength, the cavity loss was assumed constant for the five laser devices, which might not be exactly true. The slower increase in J_{th} with oscillator strength is attributed to that shorter effective lifetime of the upper lasing state ($\tau_{2,eff}$) is offset by reduced population inversion at threshold ($J_{th} = q\Delta n_{th}/\tau_{2,eff}$). As the product $f_{23} \times \tau_{23}$ remains roughly constant among the f-series devices, the evolution of threshold current density, according to this simple qualitative approach, should follow the ratio of $\tau_{23}/\tau_{2,eff}$ when diagonality (f_{23}) changes. However, the simple aforementioned effects are probably not describing very well the complexity of the dynamic range of this class of QCLs. For instance, this discussion ignores parasitic tunneling resonances that can have a large impact on laser threshold (to be described later in this section). It has been recently reported that the temperature dependence of J_{max} in THz RT-QCL simulated by a more sophisticated model (hybrid MC-DM) is not always in accordance with experiments, revealing the complexity to model QCLs under operating conditions.[47]

The maximum current density around the 1-4 anticrossing bias at 10 K was calculated with the SDM model and is plotted, somehow artificially, as a function of 1-4 anticrossing energy (AX_{14} in meV) in Figure 8(a) even though this parameter may not directly play a role in determining this leakage current. The energy splitting AX_{14} illustrates the strength of hybridization between states 1 and 4 but is not equivalent to a tunnel coupling strength. Nevertheless, to the first order of approximation, one might presume the 1-4 intermediate resonance leakage current roughly follows a form similar to the one in an incoherent tunneling transport, yielding $J_{14} = qn_s(AX_{14}/\hbar)^2(\tau_{\parallel}/2)$, where $\tau_{\parallel}$ is the tunnel dephasing time. It is straightforward to show that the anticrossing is caused indirectly via the wrong tunnel coupling strengths Ω_{13} and Ω_{24} which couple states 1 and 4 via the "up" interactions, $1 \leftrightarrow 2 \leftrightarrow 4$, and the "down" interactions, $1 \leftrightarrow 3 \leftrightarrow 4$ (Figure 1).

At the anticrossing bias, levels 1 and 4 are approximately separated before coupling by

$$\Delta_{14}^{(AX)} \approx \frac{\frac{\Omega_{12}^2 - \Omega_{24}^2}{e_2} + \frac{\Omega_{13}^2 - \Omega_{34}^2}{e_3}}{1 - \frac{\Omega_{12}^2 + \Omega_{24}^2}{2e_2^2} - \frac{\Omega_{13}^2 + \Omega_{34}^2}{2e_3^2}}, \tag{4}$$

which is positive ($E_1 > E_4$) for all designs except the f66 structure, which has a nearly vertical lasing transition. Therefore, for diagonal structures and at the anticrossing bias, the electrostatic potential per module is slightly higher than the energy spacing between the first two states of the phonon well: $E_{41'} \approx E_{LO}$, hence the anticrossing bias is as such $V_{AX} \gtrsim N \times E_{LO}/q$. In Eq. (4), Ω_{12}, Ω_{24}, Ω_{13}, and Ω_{34} are the tunnel coupling strength parameters at the anticrossing bias. Energies e_2 and e_3 stand for the ULS and LLS energies, respectively, with respect to $(E_1 + E_4)/2$, the average energy of levels 1 and 4 at the anticrossing bias; they are schematically represented in Figure 1. If the denominator of Eq. (4) is neglected and if the diagonal structures are such

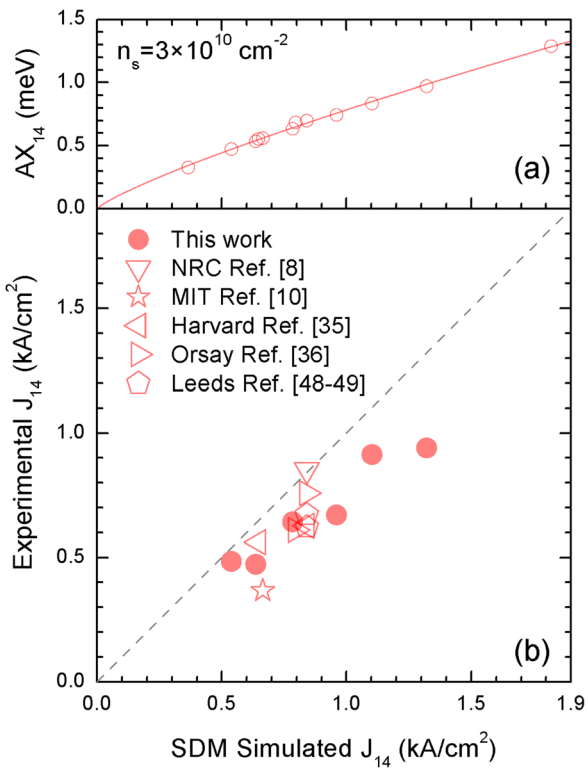

FIG. 8. (a) SDM simulated leakage current due to the intermediate resonance (J_{14}) vs. the calculated 1-4 anticrossing (AX_{14}). Several structures including the f-series devices and those published in Refs. 8, 10, 35, 36, 48, and 49 were simulated using the SDM approach. Results show that J_{14} increases superlinearly with AX_{14}. (b) Comparison between experimental data and SDM simulation results of J_{14}. The experimental data were obtained by looking at the 2nd derivative of V-J curves to find the pre-threshold shoulder that corresponds to the intermediate resonance. All experimental data were scaled in such a way that the active-region sheet doping concentration of different devices is normalized to 3×10^{10} cm^{-2}. The figure shows that the SDM model over-estimates J_{14}.

that $\Omega_{12}^2 \gg \Omega_{13}^2$ and $\Omega_{34}^2 \gg \Omega_{24}^2$, a simple approximated analytical expression of AX_{14} can thus be derived

$$AX_{14} = 2\left(\frac{\Omega_{12}\Omega_{24}}{e_2} + \frac{\Omega_{13}\Omega_{34}}{e_3}\right). \quad (5)$$

The tunnel coupling strengths Ω_{13} and Ω_{34} have opposite signs, but e_3 is negative; therefore, in due course the two terms of Eq. (5) add constructively to the anticrossing. The approximations which lead to this expression result in an estimated anticrossing 11.6%-24.4% larger than what is computed by solving the Schrödinger equation with four wells. As expected, the discrepancy continuously increases with oscillator strength. More precisely, our model (Eq. (5)) fails only for the quasi vertical structure f66 (24.4% error) while the error is reasonable for the other designs (from 18% for f47 to 11.6% for f20). Equation (5) shows that the detrimental effects of the 1-4 anticrossing will increase as the frequency of the QCL is decreased (smaller e_2 and e_3).

We used three-well THz QCL designs tested at the National Research Council Canada and several more from the literature[10,35,36,48,49] to calculate the anticrossing AX_{14} and current density J_{14} at the anticrossing bias. Results calculated at 10 K (red dots) are plotted in Figure 8(a). It shows that the 1-4 anticrossing current density (J_{14}) increases with the increase in 1-4 anticrossing (AX_{14}). As the oscillator strength (f_{ul}) increases from 0.26 to 0.47, the 1-4 anticrossing AX_{14} increases from 0.54 meV to 0.97 meV, and the corresponding J_{14} increases from $\sim$600 A/cm^2 to $\sim$1300 A/cm^2. Since the 1-4 anticrossing occurs just before the device reaches its lasing threshold, the J_{14} leakage current may contribute a significant portion of the threshold current density.[36] In Figure 8(b), experimental current densities at 1-4 anticrossing at 10 K for the 3-well devices are compared to the simulated values obtained from the SDM model. The current density (such as J_{th} and J_{max}) flowing through quantum cascade structure is proportional to the two-dimensional doping concentration.[18] We therefore use $J \times (3 \times 10^{10})$/(actual doping density) to normalize the current densities in our comparison. The wafer V812 (f30) was also measured in reverse polarity, for which $AX_{14} = 0.475$ meV, so six experimental points (red solid dots) were obtained from this work, as shown in Figure 8(b). Several groups have tested the design presented in Ref. 8; this is why Figure 8(b) shows multiple experimental points for the same simulated current density J_{14} of 840 A/cm^2. The fact that the experimental J_{14} is lower than simulated J_{14} suggests that the numerical results represent an overestimation. Since 1-4 intermediate resonant tunneling is in the incoherent regime due to the short lifetime of the extraction state 4, one would naively predict the leakage current density to follow a trend of $J_{14} \propto (AX_{14})^2$. However, the numerical simulation by SDM shows a weaker dependence: $J_{14} \propto (AX_{14})^{1.2}$ (the guiding curve in Figure 8(a)), which indicates this indirect current channel would be more complex to write analytically than the sequential resonant tunneling between two neighbour QW subbands, i.e., the Kasarinov and Suris's model.

The similarity in dependence on 1-4 anticrossing AX_{14} between the experimental J_{th} data and the numerical J_{14} results indicates the 1-4 anticrossing in the f-series devices plays an important role in device threshold current density. In order to minimize threshold current density, the 1-4 intermediate resonance should be suppressed as much as possible. One possible solution is to purposely align the injection states (1 and 2) at a higher electric field than the aligned extraction states (3 and 4). Reference 10 gave one such successful example—the injection states were aligned at 12.7 kV/cm while the extraction states were aligned at 11.2 kV/cm. In this design, at the 1-4 anticrossing the state 1 is farther away from its injection resonance than state 4 from its extraction resonance. This choice of electric field detuning ΔF_{ie} between the two resonances (injection resonance occurring 1.5 kV/cm after the extraction) is consistent with the fact that Ω_{34}, the extraction coupling, is about twice Ω_{12}, the injection coupling. In practice, it simply means it is easier to localize the mixed symmetric state between 1 and 2 behind the injection barrier than it is to localize the mixed antisymmetric state between 3 and 4 after the extraction barrier. This choice of detuning between the two resonances can also be justified by Eq. (5): the wrong extraction coupling Ω_{24} is difficult to decrease since ULS is naturally less confined than LLS; therefore, the ratio r between the average (in fact, the geometric mean) "down" coupling strength, $\Omega_{down} = \sqrt{|\Omega_{13}\Omega_{34}|}$, and the average "up" coupling, $\Omega_{up} = \sqrt{|\Omega_{12}\Omega_{24}|}$, that are represented in Figure 1, is less than unity. Table I shows the values of Ω_{up}, Ω_{down}, and r at the anticrossing electric field. The minimum anticrossing (AX_{14}) occurs at an injection detuning of

$$|\Delta_{12}|_{\min AX} \approx \frac{\Delta_{23}^{(AX)}}{1 + \frac{\Omega_{down}}{\Omega_{up}}} = \frac{\Delta_{23}^{(AX)}}{1 + r}, \quad (6)$$

which is larger than half the energy spacing between the lasing states at the anticrossing bias, $\Delta_{23}^{(AX)}/2$. In other words, if the gain and threshold current density are equally important for a particular application, it is probably preferable to align the states 1 and 4 away more from the "up" coupling than from the "down" coupling in order to minimize the impact of anticrossing even though this strategy results in a slightly decrease in gain. The ratio r, which is smaller than unity in this family of designs, confirms that the wrong injection, although not negligible, is not as critical as the wrong extraction channel. From Eq. (6) one can estimate the optimum detuning in electric field ΔF_{ie} between the injection and extraction resonances

$$\Delta F_{ie} \approx \frac{\Delta_{23}^{(AX)}}{q(1+r)}\left(\frac{1}{\delta_{21}} - \frac{r}{\delta_{43}}\right) - \frac{\Delta_{14}^{(AX)}}{2q}\left(\frac{1}{\delta_{21}} - \frac{1}{\delta_{43}}\right), \quad (7)$$

where $\delta_{ij} = z_{ii} - z_{jj}$ is the static dipole between the states i and j and $r = \Omega_{down}/\Omega_{up}$ is given at the anticrossing bias. If we assume the injection and extraction static dipoles are similar, i.e., $\delta_{21} \sim \delta_{43} \equiv \langle\delta\rangle$, detuning in the electric field can be written in a simpler form

$$\Delta F_{ie} \approx 2\frac{\hbar\omega + \Delta_{14}^{(AX)}\frac{\delta_{32}}{2\langle\delta\rangle}}{q\left(\frac{1+r}{1-r}L + \delta_{32}\right)} \approx 2\frac{1-r}{1+r}\frac{\hbar\omega}{qL}, \quad (8)$$

where $\hbar\omega$ is the energy spacing between the lasing states at the injection resonance and L is the length of a module. These two last expressions give an estimated upper bound for the allowed detuning since this technique is made at the expense of the peak gain value. For the structure presented in Ref. 10, the ratio $r = 0.717$ and the optimum resonance detuning to minimize the 1-4 anticrossing would be slightly above 1.2 kV/cm according to Eq. (7), in close agreement with the designed detuning of 1.5 kV/cm, which suggests the design is fairly optimized. The small discrepancy (~0.3 kV/cm) can be attributed to Eq. (5), which only gives an estimation of the anticrossing. This structure has the same oscillator strength as the f35 design but its J_{14} current density is 45% lower as a result of the detuning technique of the injection and extraction resonances. According to our model, this detuning technique was done at a slight expense of the gain; for instance, a $T_{max} = 173$ K is predicted for a cavity loss of 25 cm^{-1} while the key parameters of this structure are similar as that of design f35 ($\Omega_{12} = 1.152$ meV, $\Omega_{34} = 2.375$ meV, and $f_{23} = 0.35$ at 12 kV/cm for the design in Ref. 10). In the f-series designs, the SDM based optimization automatically sets the injection tunneling alignment and the extraction tunneling alignment at the same electric field, which explains why the 1-4 intermediate resonance leakage is far from being well suppressed and thus strongly influences device performance. In addition, the 1-4 intermediate resonance plays an important role in device operation stability, as will be discussed in Sec. IV C.

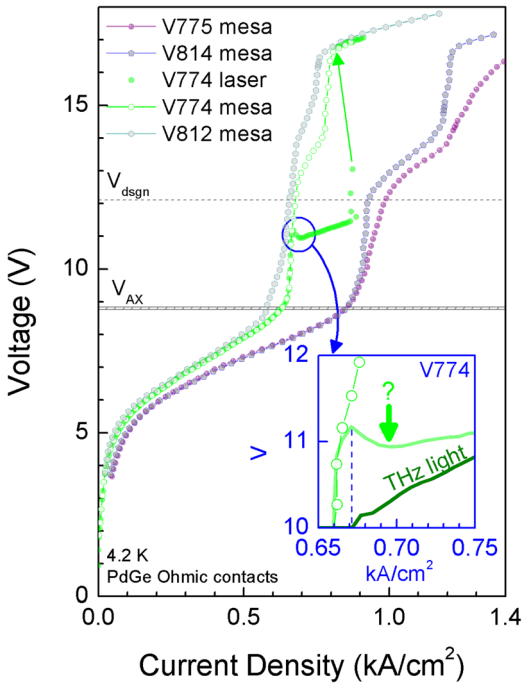

FIG. 9. Voltage vs. current density curves, measured in pulsed mode with a current source at 4.2 K, with non-lasing devices from wafers V775 (f47), V814 (f41), V774 (f35), and V812 (f30) processed as metal-metal mesas with PdGe contacts. The theoretical anticrossing voltages V_{AX} for the four structures are within the patterned horizontal band. The last three devices show very high differential resistance after the anticrossing voltage (V_{AX}), whereas V775 shows the smoothest electrical characteristics. The V-J curve of a V774 Fabry-Pérot laser with the same contact is also displayed. The inset highlights the voltage recession (marked by a vertical down arrow) at the V774 lasing threshold.

C. Operation instability and high field domain

The feature associated with the 1-4 intermediate resonance is explicitly observable in the transport characteristics of the f-series devices. Figure 9 shows the voltage (V)–current density (J) curves of metal-metal non-lasing mesas (from V775 (f47), V814 (f41), V774 (f35), and V812 (f30)) and a lasing ridge (from f35), where both types of devices were processed with top and bottom PdGe Ohmic contacts.[22] Looking at the f35 (V774) devices, both V-J curves exhibit a current plateau at a current density of ~0.66 kA/cm^2, which is just before the lasing threshold point, as clearly revealed in the inset of the zoomed-in V-J curves near the lasing threshold. This current plateau (impeded current flow) is caused by the injection state 1 passes over the extraction state 4 (off resonant) when the bias goes beyond the 1-4 anticrossing (~8.8 kV/cm).

For the f35 lasing device, the onset of stimulated emission opens up a new carrier transport channel—a designed lasing channel that consists of 1-2 injection resonant tunneling, 2-3 stimulated radiative relaxation, and 3-4 extraction resonant tunneling. As a result, the device resistance drops upon the inception of lasing operation. In addition, we even observe a reproducible small decrease in voltage at the beginning of laser operation, which suggests the electric field profile is reconfigured across the active region. This new effect was revealed unambiguously on an oscilloscope and was systemically observed on all f41, f35, f30, and f26 laser devices. The V-J curve exhibits a linear increasing section through the whole lasing dynamic range. The above-threshold differential resistance is very small, $R_{ac} = \sim 1.5\text{-}2\ \Omega$, which is a sign of coherent transport through the injection barrier towards the upper lasing state in conjunction with the short lifetime of the LLS.[46]

In contrast, the V-J curve of the non-lasing f35 device does not show any resonance characteristics associated with the 1-2 and 3-4 level alignments. While there is no clear explanation, this may be attributed to the slow 2-3 non-radiative processes and reduced wrong coupling Ω_{24}. Later in this section, we put forward a hypothesis that the strong 1-4 intermediate resonance could mask subsequent resonances if they are not substantially stronger than the 1-4 resonance. The resonance feature at biases ~14 V is observed in f47, f41, f35, and f30 non-lasing devices (see Figure 9) and is attributed to the resonant alignment of the injection state 1 to higher energy states situated two modules away in the downstream direction. At high biases beyond 16-17 V, a leakage path to continuous band emerges and the current density starts to increase quickly with bias again.

The V774 (f35 design) lasing device exhibited a negative differential resistance (NDR) at a current density of ~0.87 kA/cm^2, and the subsequent lasing operation was quenched as both 1-2 and 3-4 resonant tunneling was strongly suppressed. Interestingly the electric field profile inside the active region of the lasing device automatically reconfigured itself and the device bias jumped to the next stable operation point in a positive differential resistance (PDR) region. This corresponds to the initiation of the carrier

leakage to the aforementioned continuous band. This electric field automatic renormalization is necessary to ensure the continuity of current flow. The carriers were automatically channelled into the next available current channel with sufficient capacity to support the same/comparable current density during this renormalization process.

The electric field reconfiguration right at the lasing threshold was actually observed in all f-series lasing devices. Figure 10 shows V-J curves of the f-series lasing devices at 10 K. Current plateaus are observed in all five curves at their respective threshold points. The current plateau becomes more substantial as the oscillator strength decreases. More interestingly, the threshold voltage of f26 (at which point the lasing is initiated) is 15 V at 10 K, which is much higher than the design bias (12 V). This, together with the device electrical instability that will be discussed shortly, is closely related to the competition/switching of two (or more) different current-carrying channels, more specifically, the 1-4 intermediate resonance (1-4 anticrossing) leakage channel and the designed lasing channel.

As diagonality increases (oscillator strength decreases), the current-carrying capacity through both transport channels drops. For example, the $J_{th} \sim 0.51\,kA/cm^2$ of the f26 device is the lowest, and its injection coupling strength ($\Omega_{12} = 1.231$ meV) and extraction coupling strength ($\Omega_{34} = 2.021$ meV) are also the smallest among all five devices. Our SDM simulations show that the current-carrying capacity at the design bias (12 kV/cm), including the designed lasing channel ($1 \rightarrow 2 \rightarrow 3 \rightarrow 4$) and the wrong extraction channel ($1 \rightarrow 2 \rightarrow 4$), decreases relatively faster than that of the 1-4 anticrossing channel when the diagonality increases. As a result, when the current-carrying channel switches from the 1-4 anticrossing channel to the designed lasing channel, extra externally applied bias is needed to compensate the relatively lower current-carrying capacity of the designed lasing channel, and this additional bias becomes larger in a more diagonal device, i.e., the next stable operating point with PDR is dragged to higher voltages. The internal electric field profile reconfiguration thus occurs at a higher bias, leading to a wider current plateau in a device with a lower oscillator strength.

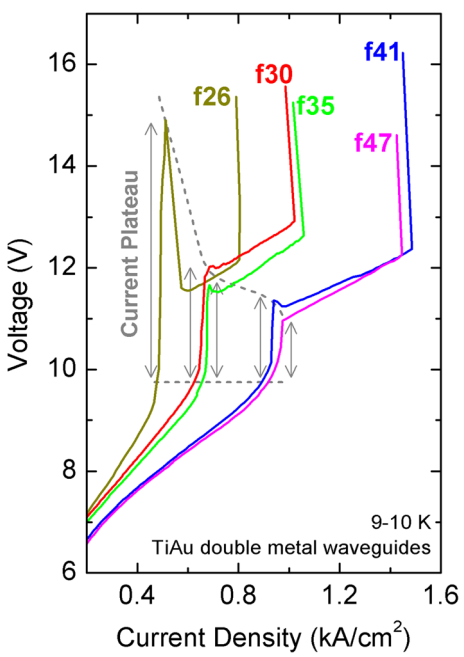

FIG. 10. V-J curves of f-series lasing devices at 9-10 K where the current plateau before threshold is emphasized.

The experimental observations (the pre-threshold current plateaus, the small voltage drop (recession) after the threshold, and the higher-than-expected threshold voltage in the f26 device) might be explained by assuming the formation of high electric-field domains (EFDs) across the active region. Figure 11 presents diagrams that illustrate this hypothesis. The bottom diagram of Figure 11(a) shows schematic J-F curves (current density-electric field) for devices with higher oscillator strengths with lasing off (solid black) and on (dash green). These curves represent the current-carrying capacity of different channels. In this sketch, the entity F_{appl} denotes the average electric field applied to the device (V_{appl}/NL). The two peaks correspond to the two current-carrying channels, with the 1-4 anticrossing leakage channel at the lower bias ($F_{AX} \sim 8.8$ kV/cm) and the designed lasing channel and the wrong extraction channel at the higher bias ($F_{dsgn} \sim 12$ kV/cm). Note that the current-carrying capacity through the designed lasing channel and the wrong extraction channel in the device represented in Figure 11(a) is greater than that of the 1-4 anticrossing channel, even when the device is in the lasing off state ($J_{max} > J_{14}$). We also recall that in most of our experiments, the devices are driven in current mode, where a load of 44 Ω is used in series with the QCL device, rather than in voltage mode.

When transport is controlled by interwell tunneling with weak coupling between the wells, the devices will very likely show sawtooth-like I-V curve with a voltage source because of the formation of EFDs.[50–55] EFDs have been used to explain the sawtooth-like L-V and I-V curves obtained from THz QCLs driven in voltage mode,[55] and the hypothesis we put forward here was inspired by this previous work. Beyond the 1-4 anticrossing, the current flow through the 1-4 anticrossing channel started to drop with further increases in device bias. In order to maintain current flow continuity, a higher-field domain started to develop from the side close to the top contact layer. The quantum cascade modules near the bottom contact layer were pinned at the 1-4 anticrossing electric field while all extra bias was applied to the cascade modules in the growing electric-field domain. As such, the current flowing through the active region was bound by the maximum current-carrying capacity of the 1-4 anticrossing channel, but the total device bias continuously increased as more and more modules switched from the lower EFD to the higher EFD. This led to the formation of a current plateau right before the threshold. In f-series QCLs, we believe the domains are more robust when the anticrossing AX_{14} decreases and when the next stable operating point in voltage, i.e., the point with the same current as J_{14} with PDR (see the PDR spot in Figure 11) is farther away in voltage than that of anticrossing.

When sufficient cascaded modules switched to the higher EFD in which carriers were injected into the upper lasing state and population inversion was built up, the accumulative optical gain from the higher EFD modules

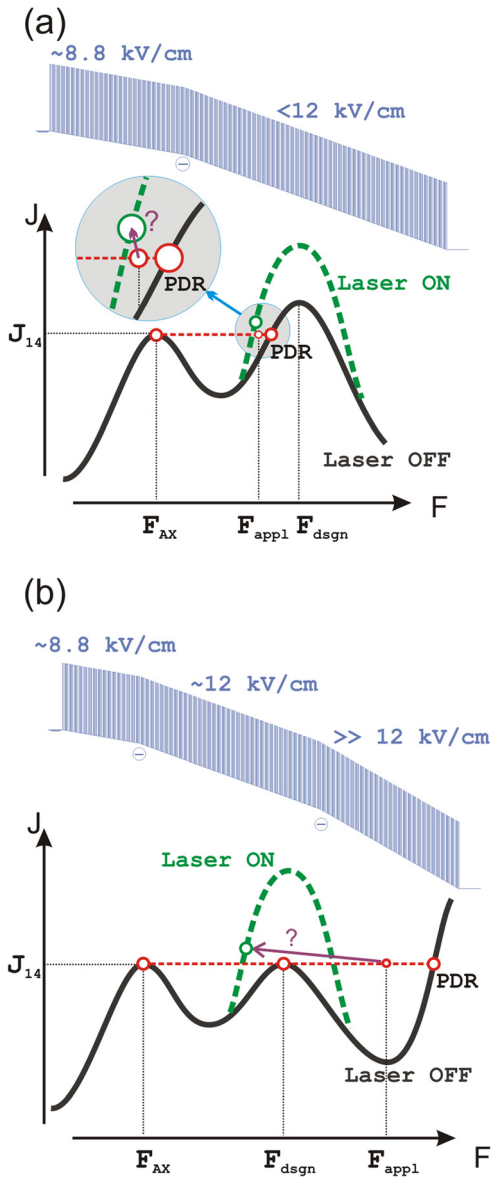

FIG. 11. Illustrations of a hypothesis based on the formation of high-field domains across the 10 μm thick active region, which may explain the voltage recession at laser threshold. (a) Devices with higher oscillator strengths. (b) Devices with lower oscillator strengths. Note that the operating bias point transition from the laser-off state to the laser-on state.

eventually overcame the waveguide loss, leading to the inception of stimulated emission. Once lasing was initiated, current-carrying capacity through the designed lasing channel was significantly enhanced due to fast stimulated radiative relaxation from the upper to the lower lasing states. We hypothesize that when the higher EFD conductance increases through the stimulated emission process, the electric field is eventually and quickly reconfigured through the entire active region and becomes uniform (one domain). The operating point would then fall on the lasing J-F curve, as schematically represented by the dashed green line in Figure 11(a). It would require slightly lower bias to carry the same amount of current density. The operating bias point of individual cascade modules gradually shifted from the red spot to the green spot in the zoomed-in section of Figure 11(a). That explains the observed device voltage recession upon/after the lasing emission. The overall device voltage continued to drop until the stimulated emission was excited across the all/most cascaded modules. This could explain the gradual voltage drop after the lasing threshold, as observed in the f-series devices. Sometimes, the voltage recession can occur in several steps, suggesting the electric field does not switch to the design value ($\sim F_{dsgn}$) in all the modules at the same average electric field; in other words, lasing is possible with several EFDs. This effect is nicely evident in Figure 12(c), which shows V-J curves for the f35 device at temperatures of 10 K and 70 K where the voltage seems stabilized after the first recession, while a second voltage recession occurred at a current density that is 97 A/cm^2 (10 K) and 176 A/cm^2 (70 K) higher than their threshold points, respectively. After the second voltage recession it is believed the electric field is uniform across the active region; however, more experiments are required to confirm this.

As shown in Figure 10, no voltage dip after the current plateau is observable in the f47 device curve. It is not yet clear why the f47 device does not show a voltage setback at threshold; thus, we are limited to qualitative explanations. One could claim that among the series of grown wafers, the f47 structure has a highest current-carrying capacity around the design electric field; hence, the valley in the J-V characteristic might be not as pronounced as in Figure 11(a). In other words, it is possible that the first point in the dashed green curve in Figure 11(a) is not below the current at anticrossing, J_{14}. This explanation seems to be supported by the V-J curves displayed in Figure 9. The electrical characteristic is rather smooth for V775 with a clear PDR behaviour at the design voltage (V_{dsgn}). This latter observation for V775 should be opposed to the electrical characteristics that are more irregular for highly diagonal structures and which show large differential resistance at design voltage: this is a sign that current-carrying capacity at V_{dsgn} of diagonal structures ($f_{ul} \leq 0.41$) is only marginally higher than J_{14}. One might also claim the EFDs are not as robust in f47 since the structure is naturally more conductive because it has a stronger overlap between the lasing states, a more pronounced wrong extraction leakage channel and a larger anticrossing. As a result, we should immediately find the stable PDR point on the lasing J-V.

To go beyond these qualitative explanations, more experimental studies are required to get a better picture of the electric field distribution with and without stimulated emission. For instance, J-V measurements of very small non-lasing devices in voltage mode are recommended. Gain measurements on non-lasing devices might be useful too to confirm the population inversion above the anticrossing voltage and to understand the resonance at ~14 V.

For devices with lower oscillator strengths, the situation is more complicated because the peak current-carrying capacity through the design lasing channel and the wrong extraction channel in the lasing-off state is rather limited. Thus, a third current-carrying channel might be involved. The third current carrying channel is likely the parasitic leakage path to the continuous band, which occurs at a much higher electric field (16–17 kV/cm). Similar to what happened in devices with higher oscillator strengths, EFDs developed and current channels switched in devices with lower

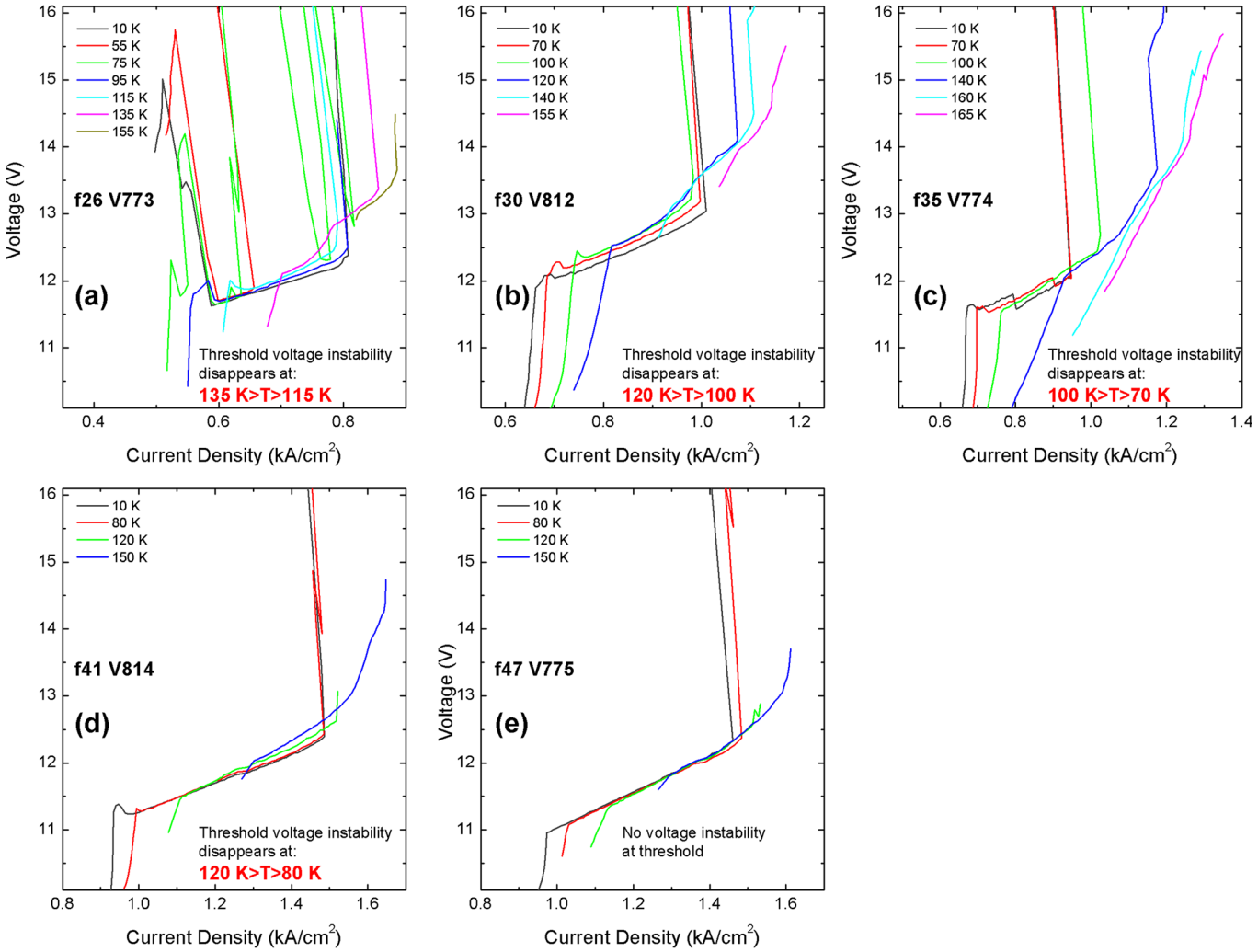

FIG. 12. J-V curves of f-series devices at different temperatures. The voltage recession after the threshold changes with temperature and disappears at higher temperatures.

oscillator strengths. But now, the difference might be that three different EFD zones could coexist inside the 10 μm thick active region.[54] As shown in Figure 11(b), the zone close to the bottom contact layer remained in the lower EFD region (~8.8 kV/cm), the zone close to the top contact layer entered into a much higher EFD region (~16–17 kV/cm), and the middle zone stayed around the design electric field (~12 kV/cm). As the bias grew, the middle EFD zone expanded and eventually accumulated enough gain to kick off stimulated emission. As long as the lasing was initiated, the operating status of all quantum cascade modules began to shift towards the green spot on the dashed green curve, corresponding to the design lasing channel in the lasing-on state. The electric field profile across the active region reconfigured (one domain) and the overall device bias dropped.

Depending on the oscillator strength, the peak current-carrying capacities through the designed lasing channel and the wrong extraction channel in the lasing off state vary, leading to a different partition in the high-field domains across the whole active region. For the f26 device, a good portion of the cascaded modules of the 10 μm thick active region could be in the higher EFD of 16–17 kV/cm prior to the lasing threshold. As a result, the f26 pre-threshold current plateau and the above-threshold voltage recession are the most pronounced among all five f-series devices.

Diagonality plays different roles in determining the current-carrying capacity through the different channels. In the f-series designs, three current-carrying channels—the intermediate resonance channel ($1 \rightarrow 4$), the designed lasing channel ($1 \rightarrow 2 \rightarrow 3 \rightarrow 4$), and the wrong extraction channel ($1 \rightarrow 2 \rightarrow 4$)—are the most important because device performance is strongly influenced by the competition between these three channels. As shown in Figure 8, the leakage current through the intermediate resonance channel (J_{14}) exhibits an almost linear dependence on the oscillator strength ($J_{14} \propto (AX_{14})^{1.2}$) rather than a quadratic dependence on AX_{14} as should be expected in an incoherent tunneling scheme. J_{14} drops by a factor of ~3.9 as the oscillator strength decreases from 0.66 to 0.20. On the other hand, the current-carrying capacity through the designed channel at the design bias drops only by a factor of ~3 based on a simple back-of-the-envelope calculation for the same proportion. This is attributed to the longer upper lasing state lifetime for more diagonal structures.

For the same diagonality range, the wrong extraction coupling strength (Ω_{24}) reduced by almost a factor of 5, from

2.903 meV down to 0.613 meV as shown in Table I. As a result, the current-carrying capacity through the wrong extraction channel at the design bias (12 kV/cm) drops much faster than J_{14} as the diagonality increases. Returning to the SDM model, when the designed channel and the wrong extraction channel are combined, the current-carrying capacity at 12 kV/cm exhibits a faster drop (÷4.76) than that of the intermediate resonance at ~8.8 kV/cm (÷3.9) as the oscillator strength decreases from 0.66 to 0.20. This is inline with the hypothesis as shown in Figure 11, and our experimental observations, namely, (i) stable operation of f47 lasing devices and unstable f26 devices; (ii) the smooth V-J curves of a non-lasing f47 devices in opposition with the high differential resistance observed at design voltage on more diagonal structures (see Figure 9). We therefore see the importance to spatially separate the upper lasing state from the downstream extractor/injector states for the purpose of suppressing the leakage current through $2 \rightarrow 4 \rightarrow 1'$ channel. Apparently, by increasing diagonality in the design, the threshold current density decreases. However, there are two effects that must be kept in mind: (a) the parasitic leakage current at 1-4 anticrossing (J_{14}) does not drop as fast as expected and (b) the parasitic leakage current through the wrong extraction channel ($2 \rightarrow 4$) drops at a much faster pace. Combined, these two effects could push the device into a dangerous zone where the current-carrying capacity at 1-4 anticrossing (J_{14}) becomes higher than that at the designed bias (~12 V), as illustrated in Figure 11(b). This could lead to instable operation and even quench lasing activity completely.

The competition/switching of current-carrying channels is a recognized limitation of the kind of resonant tunneling-based designs. It can cause serious problems, especially for THz QCLs with longer lasing wavelengths.[3] In Ref. 3, it was explained that the tunneling resonance in a 3-level RT-QCL between the injector state 1 and the lower lasing state 3 imposes an upper bound for the injection coupling strength Ω_{12} in order to maintain electrical stability. In a 4-level RT-QCL the dangerous resonance occurs between levels 1 and 4, and this study shows the important risks associated with this resonance. We experimentally observed device operation instability of the f-series devices, which is attributed to current-carrying channel competition/switching and EFD formation.

Figure 12 shows the J-V curves of the f-series devices at different temperatures. For the f26 device, voltage instability is so prominent at lower temperatures such as 55 K and 75 K. For example, the 75 K curve for this device displays a few abrupt voltage jumps from high to low or vice versa as the current density increases. Each of these voltage jumps corresponds to a switch-on or a switch-off of the laser emission (Figure 3(a)). These jumps in voltage and light can be attributed to the aforementioned formation of EFDs, and the difficulty in suppressing the EFDs—in other words, to stabilize the electrical circuitry—with laser emission. At the end of the lasing dynamic range, the voltage jumped from the design bias to a much higher bias, the current slightly decreased and the lasing emission dropped sharply to almost zero. The voltage recession that occurred immediately after lasing threshold (in the J-V curves) was observed for all devices (except f47) at low temperatures but disappeared at higher temperatures. The f47 device shows no voltage recession at any temperature between 10 K and 180 K (T_{max}). The voltage recession becomes imperceptible at a temperature T_{res} between 80 and 120 K for the f41 device, 70-100 K for the f35 device, 100-120 K for the f30 device, and 115-135 K for the f26 device. This uncertainty on T_{res} is due to the coarse temperature scan during the measurement campaign; nevertheless, we can safely affirm there is a general trend of increase in T_{res} with diagonality. This temperature dependence of the voltage recession on device oscillator strength is related to the competition among different current-carrying channels. We think the voltage recession disappears when the current–carrying capacity of the designed lasing channel becomes comparable to, and preferably larger than, that of the 1-4 anticrossing channel. The f26 device demonstrates the lowest current-carrying capacity through the designed lasing channel; therefore, a higher temperature is needed to equalize the current-carrying capacities through the designed lasing channel and the 1-4 anticrossing channel.

At higher temperatures, the designed lasing channel can conduct a higher current and eventually will make the 1-4 anticrossing channel less dominant. The light emission and carrier transport property of the devices are therefore more stable at higher temperatures, as observed in the f26 to f41 devices (Figure 12). For the f47 device, the designated lasing channel carries more current because it has a shorter upper lasing state lifetime and overwhelms the 1-4 anticrossing channel. Since the current channel competition was effectively suppressed, f47 device operation performance was stable, even at 10 K. The structure presented in Ref. 10 with the 1.5 kV/cm detuning between the injection and extraction level alignment guarantees an even better stability by lowering the J_{14} contribution.

The formation of EFDs in quantum devices reportedly leads to sawtooth-like I-V curves with N-1 small spikes in the current.[50–55] We have attempted to measure sawtooth features in the I-V curves obtained from the f-series lasers, which would then confirm the EFDs. Figure 13 shows the DC I-V curve, measured with a voltage source, at 4.2 K of a small mesa ($68 \times 101\ \mu m^2$) device made from wafer V812 (corresponding to the f30 device) with PdGe Ohmic contacts. The differential resistance ($R_{ac} = dV/dI$) is also shown. The zoomed-in I-V section above the 1-4 anticrossing appears "bumpy," the corresponding R_{ac} beyond the 1-4 anticrossing voltage (~8.9 V) appears much more noisy compared to the region below the 1-4 anticrossing resonance. We note the differential resistance appears "noisy" as soon as the applied voltage is above the 1-4 anticrossing condition. This might indicate the individual cascade modules were switching between two different EFDs, and, consequently, the design lasing channel and the parasitic 1-4 anticrossing leakage channel were on and off in these transition modules, which are situated at the boundary of two EFDs. Since the current-carrying capacity of these two channels is different, the channel switching of individual cascade modules leads to observed fluctuations in the macroscopic differential resistance. Unfortunately, in this measurement, the current is still much too high to properly observe the expected sawtooth

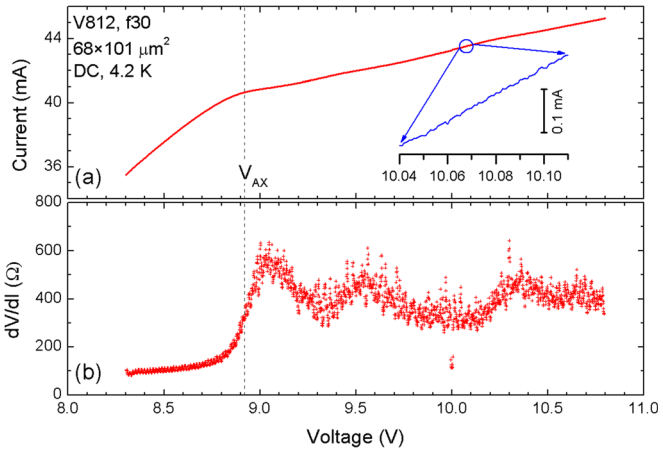

FIG. 13. (a) DC I-V curve of a small mesa device with PdGe Ohmic contacts made from wafer V812 (f30 device) at 4.2 K. The bottom plot (b) shows the differential resistance dV/dI. The position of the dashed vertical line corresponds to the maximum second derivative, i.e., the anticrossing bias.

features, and a special photolithography mask would be required to fabricate much smaller devices.

Although the experimental observations can be explained by and/or are consistent with our hypothesis of high-field domain formation and current-carrying capacity of different channels, which was inspired by earlier work on electric-field domains in THz QCLs,[55] the dynamics of EFD formation and switching is still not clear. The photoluminescence spectroscopy[52,53] and/or new technology such as scanning voltage microscopy[56,57] could be employed to provide direct evidence of this hypothesis and provide further insight into its dynamic behaviours.

V. CONCLUSIONS

A series of resonant phonon-based terahertz quantum cascade lasers were designed and fabricated in a lasing frequency range of 3.2-3.7 THz. The quantum active regions of the devices were designed and optimized using a simplified density matrix formalism, in which a few oscillator strengths from 0.26 to 0.47 were selected. The effect of oscillator strength on the performance of these SDM optimized structures was investigated in a systematic manner. The experimental results show that the maximum lasing temperature (T_{max}) of the devices did not demonstrate a strong dependence on the oscillator strength (radiative transition diagonality), but the threshold current density was reduced significantly as diagonality increased. Lower threshold current density was achieved in more diagonal structures, which is attributed to that the leakage current due to intermediate tunneling resonance (1-4), and other parasitic leakage channels are more effectively suppressed. Nevertheless, the current-carrying capacity of the designed lasing channel was diminished at an even faster rate as diagonality increases. At a certain point, lowering the oscillator strength leads to the leakage current at the intermediate resonance become comparable to or even overwhelm the designed lasing channel, causing development of electric-field domains and the competition/switching of current-carrying channels. Electrical instability was experimentally observed in the fabricated lasing devices. One important lesson drawn from the study is that the leakage through intermediate resonance and other parasitic channels should be carefully minimized to avoid development of electric-field domains when designing a quantum active region to achieve high temperature operation.

ACKNOWLEDGMENTS

The authors warmly thank Christoph Deutsch from TU Vienna for stimulating discussions and would like to acknowledge support from Natural Science and Engineering Research Council (NSERC) of Canada, from Canadian Foundation of Innovation (CFI), from the Ontario Research Fund (ORF), and from CMC Microsystems. H.C.L. thanks National Major Basic Research Program (2011CB925603) and Natural Science Foundation of China (91221201 and 61234005) for their generous funding contributions. The work at MIT is supported by NASA and NSF.

APPENDIX: HIGH TEMPERATURE PERFORMANCE OF f30 DESIGN

The f30 wafer (V812) was processed at MIT as a Cu double metal ridge waveguide in the same way as the device with $T_{max} = 199.5$ K described in Ref. 23. The L-J characteristics and spectra of this device are plotted in Figure 14. This lower loss waveguide resulted in higher temperature performance ($T_{max} = 199.3$ K) as compared to its counterpart with a Au-Au ridge waveguide ($T_{max} = 160$ K). This effect has been attributed to the smaller temperature sensitivity of the optical gain for very diagonal lasing transitions (Figures 1 and 6). At 8 K the relative dynamic range is 54%, in other words, substantially higher than in Au-Au waveguides (34%, see

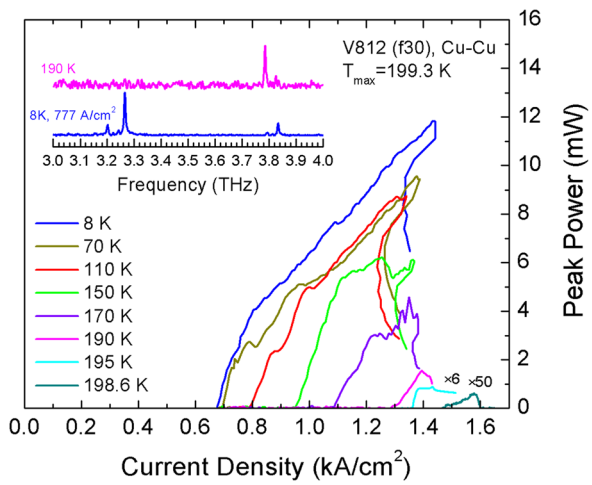

FIG. 14. L-J curves of a V812 QCL device (f30) with a Cu-Cu waveguide at different temperatures. The maximum lasing temperature of this device is 199.3 K, which is just slightly lower than $T_{max} = 199.5$ K from a QCL device made from V775 (f47) wafer reported in Ref. 23. Nevertheless, the threshold current of this device is significantly lower (−31%), $J_{th} = 0.675$ kA/cm^2 (f30 device) vs. 0.975 kA/cm^2 (f47 device) at 8 K. The inset shows the lasing spectra of the f30 device with a Cu-Cu waveguide at 9 K and 190 K. The single peak lasing frequency at 190 K of this Cu-Cu QCL device is close to that of the f30 device with a Au-Au waveguide. However, at low temperatures, the lasing spectrum of the Cu-Cu device spans over a much wider range than that of the Au-Au device.

Figures 3(b) and 5(b)). This improvement has been achieved by a 44% increase in J_{max} while the threshold current density stayed unchanged because the latter is determined by the parasitic current channel J_{14}.

[1]R. Kohler, A. Tredicucci, F. Beltram, H. E. Beere, E. H. Linfield, A. G. Davies, D. Ritchie, R. C. Iotti, and F. Rossi, "Terahertz semiconductor-heterostructure laser," Nature (London) **417**, 156–159 (2002).

[2]N. Horiuchi, "Chasing room temperature," Nat. Photonics **6**, 213 (2012).

[3]S. Kumar, C. W. I. Chan, Q. Hu, and J. L. Reno, "A 1.8-THz quantum cascade laser operating significantly above the temperature of $\hbar\omega/k_B$," Nat. Phys. **7**, 166–171 (2011).

[4]M. Tonouchi, "Cutting-edge terahertz technology," Nat. Photonics **1**, 97 (2007).

[5]S. Barbieri, J. Alton, H. E. Beere, E. H. Linfield, D. A. Ritchie, S. Withington, G. Scalari, L. Ajili, and J. Faist, "Heterodyne mixing of two far-infrared quantum cascade lasers by use of a pointcontact Schottky diode," Opt. Lett. **29**, 1632–1634 (2004).

[6]J. R. Gao, J. N. Hovenier, Z. Q. Yang, J. J. Baselmans, A. Baryshev, M. Hajenius, T. M. Klapwijk, A. J. L. Adam, T. O. Klaassen, B. S. Williams, S. Kumar, Q. Hu, and J. L. Reno, "A terahertz heterodyne receiver based on a quantum cascade laser and a superconducting bolometer," Appl. Phys. Lett. **86**, 244104 (2005).

[7]B. S. Williams, S. Kumar, Q. Hu, and J. L. Reno, "Operation of terahertz quantum-cascade lasers at 164 K in pulsed mode and at 117 K in continuous-wave mode," Opt. Express **13**, 3331–3339 (2005).

[8]H. Luo, S. R. Laframboise, Z. R. Wasilewski, and H. C. Liu, "Terahertz quantum cascade lasers based on a three-well active module," Appl. Phys. Lett. **90**, 041112 (2007).

[9]M. A. Belkin, J. A. Fan, S. Hormoz, F. Capasso, S. P. Khanna, M. Lachab, A. G. Davies, and E. H. Linfield, "Terahertz quantum cascade lasers with copper metal-metal waveguides operating up to 178 K," Opt. Express **16**, 3242–3248 (2008).

[10]S. Kumar, Q. Hu, and J. L. Reno, "186 K operation of terahertz quantum cascade lasers based on a diagonal design," Appl. Phys. Lett. **94**, 131105 (2009).

[11]R. W. Adams, K. Vijayraghavan, Q. J. Wang, J. Fan, F. Capasso, S. P. Khanna, A. G. Davies, E. H. Linfield, and M. A. Belkin, "GaAs/Al0.15Ga0.85As terahertz quantum cascade lasers with double-phonon resonant depopulation operating up to 172 K," Appl. Phys. Lett. **97**, 131111 (2010).

[12]S. Kumar, C. W. I. Chan, Q. Hu, and J. L. Reno, "Two-well terahertz quantum-cascade laser with direct intrawell phonon depopulation," Appl. Phys. Lett. **95**, 141110 (2009).

[13]G. Scalari, M. I. Amanti, C. Walther, R. Terazzi, M. Beck, and J. Faist, "Broadband THz lasing from a photon-phonon quantum cascade structure," Opt. Express **18**, 8043–8052 (2010).

[14]A. Wacker, "Extraction-controlled quantum cascade lasers," Appl. Phys. Lett. **97**, 081105 (2010).

[15]H. Luo, S. R. Laframboise, Z. R. Wasilewski, and H. C. Liu, "Effects of injector barrier on performance of terahertz quantum-cascade lasers," IEE Electron. Lett. **43**, 633–635 (2007).

[16]H. Luo, S. R. Laframboise, Z. R. Wasilewski, H. C. Liu, and J. C. Cao, "Effects of extraction barrier width on performance of terahertz quantum-cascade lasers," IEE Electron. Lett. **44**, 630–631 (2008).

[17]H. C. Liu, M. Wächter, D. Ban, Z. R. Wasilewski, M. Buchanan, G. C. Aers, J. C. Cao, S. L. Feng, B. S. Williams, and Q. Hu, "Effect of doping concentration on the performance of terahertz quantum-cascade lasers," Appl. Phys. Lett. **87**, 141102 (2005).

[18]A. M. Andrews, A. Benz, C. Deutsch, G. Fasching, K. Unterrainer, P. Klang, W. Schrenk, and G. Strasser, "Doping dependence of LO-phonon depletion scheme THz quantum-cascade lasers," Mater. Sci. Eng. B **147**, 152–155 (2008).

[19]L. Ajili, G. Scalari, M. Giovannini, N. Hoyler, and J. Faist, "Doping in quantum cascade lasers. II. $GaAs/Al_{0.15}Ga_{0.85}As$ terahertz devices," J. Appl. Phys. **100**, 043102 (2006).

[20]B. S. Williams, H. Callebaut, S. Kumar, Q. Hu, and J. L. Reno, "THz quantum cascade laser at $\lambda \approx 100$ μm using metal waveguide for mode confinement," Appl. Phys. Lett. **83**, 2124–2126 (2003).

[21]Q. Hu, B. S. Williams, S. Kumar, H. Callebaut, S. Kohen, and J. L. Reno, "Resonant-phonon-assisted THz quantum-cascade lasers with metal–metal waveguides," Semicond. Sci. Technol. **20**, S228–S236 (2005).

[22]S. Fathololoumi, E. Dupont, S. G. Razavipour, S. R. Laframboise, G. Parent, Z. Wasilewski, H. C. Liu, and D. Ban, "On metal contacts of terahertz quantum-cascade lasers with a metal-metal waveguide," Semicond. Sci. Technol. **26**, 105021 (2011).

[23]S. Fathololoumi, E. Dupont, C. Chan, Z. Wasilewski, S. Laframboise, D. Ban, A. Mátyás, C. Jirauschek, Q. Hu, and H. C. Liu, "Terahertz quantum cascade lasers operating up to ~200 K with optimized oscillator strength and improved injection tunneling," Opt. Express **20**, 3866 (2012).

[24]R. Terrazi and J. Faist, "A density matrix model of transport and radiation in quantum cascade lasers," New J. Phys. **12**, 033045 (2010).

[25]S. Kumar and Q. Hu, "Coherence of resonant-tunneling transport in terahertz quantum-cascade lasers," Phys. Rev. B **80**, 245316 (2009).

[26]E. Dupont, S. Fathololoumi, and H. C. Liu, "Simplified density matrix model applied to three-well terahertz quantum cascade lasers," Phys. Rev. B **81**, 205311 (2010).

[27]S. C. Lee and A. Wacker, "Nonequilibrium Greens function theory for transport and gain properties of quantum cascade structures," Phys. Rev. B **66**, 245314 (2002).

[28]T. Kubis, C. Yeh, P. Vogl, A. Benz, G. Fasching, and C. Deutsch, "Theory of nonequilibrium quantum transport and energy dissipation in terahertz quantum cascade lasers," Phys. Rev. B **79**, 195323 (2009).

[29]T. Schmielau and M. Pereira, "Nonequilibrium many body theory for quantum transport in terahertz quantum cascade lasers," Appl. Phys. Lett. **95**, 231111 (2009).

[30]H. Callebaut, S. Kumar, B. S. Williams, Q. Hu, and J. L. Reno, "Analysis of transport properties of terahertz quantum cascade lasers," Appl. Phys. Lett. **83**, 207–209 (2003).

[31]H. Callebaut and Q. Hu, "Importance of coherence for electron transport in terahertz quantum cascade lasers," J. Appl. Phys. **98**, 104505 (2005).

[32]C. Jirauschek and P. Lugli, "Monte-Carlo-based spectral gain analysis for terahertz quantum cascade lasers," J. Appl. Phys. **105**, 123102 (2009).

[33]A. Mátyás, M. A. Belkin, P. Lugli, and C. Jirauschek, "Temperature performance analysis of terahertz quantum cascade lasers: Vertical versus diagonal designs," Appl. Phys. Lett. **96**, 201110 (2010).

[34]Y. J. Han, W. Feng, and J. C. Cao, "Optimization of radiative recombination in terahertz quantum cascade lasers for high temperature operation," J. Appl. Phys. **111**, 113111 (2012).

[35]M. A. Belkin, Q. J. Wang, C. Pflugl, A. Belyanin, S. P. Khanna, A. G. Davies, E. H. Linfield, and F. Capasso, "High-temperature operation of terahertz quantum cascade laser sources," IEEE Sel. Top. Quantum Electron. **15**, 952–967 (2009).

[36]Y. Chassagneux, Q. J. Wang, S. P. Khanna, E. Strupiechonski, J.-R. Coudevylle, E. H. Linfield, A. G. Davies, F. Capasso, M. A. Belkin, and R. Colombelli, "Limiting factors to the temperature performance of THz quantum cascade lasers based on the resonant-phonon depopulation scheme," IEEE Trans. Terahertz Sci. Technol. **2**, 83–92 (2012).

[37]A. Mátyás, R. Chashmahcharagh, I. Kovacs, P. Lugli, K. Vijayraghavan, M. A. Belkin, and C. Jirauschek, "Improved terahertz quantum cascade laser with variable height barriers," J. Appl. Phys. **111**, 103106 (2012).

[38]Z. Wasilewski, E. Dupont, D. Ban, A. Mátyás, and M. Belkin, private communication (2012).

[39]M. A. Talukder and C. R. Menyuk, "Temperature-dependent coherent carrier transport in quantum cascade lasers," New J. Phys. **13**, 083027 (2011).

[40]M. S. Vitiello, G. S. V. Spagnolo, B. S. Williams, S. Kumar, Q. Hu, and J. L. Reno, "Measurement of subband electronic temperatures and population inversion in THz quantum-cascade lasers," Appl. Phys. Lett. **86**, 111115 (2005).

[41]Y. Yao, Z. Liu, A. J. Hoffman, K. J. Franz, and C. F. Gmachl, "Voltage tunability of quantum cascade lasers," IEEE J. Quantum Electron. **45**, 730–736 (2009).

[42]T. Liu, K. E. Lee, and Q. J. Wang, "Microscopic density matrix model for optical gain of terahertz quantum cascade lasers: Many-body, nonparabolicity, and resonant tunneling effects," Phys. Rev. B **86**, 235306 (2012).

[43]T. V. Dinh, A. Valavanis, L. J. M. Lever, Z. Ikonić, and R. W. Kelsall, "An extended density matrix model applied to silicon-based terahertz quantum cascade lasers" Phys. Rev. B **85**, 235427 (2012).

[44]D. Burghoff, C. Wang, I. Chan, Q. Hu, and J. Reno, "Gain measurements of scattering-assisted terahertz quantum cascade lasers," Appl. Phys. Lett. **100**, 261111 (2012).

[45]During the processing of this wafer, the etch stop layer failed resulting to the partial etching of the active region. Besides, the mesa definition via wet-etch had photoresist adhesion problems so much that the die was extensively damaged.

[46]S. Kumar, Ph.D. dissertation, MIT, Cambridge, USA, 2007.

[47]I. Bhattacharya, C. W. I. Chan, and Q. Hu, "Effects of stimulated emission on transport in terahertz quantum cascade lasers based on diagonal designs," Appl. Phys. Lett. **100**, 011108 (2012).
[48]S. P. Khanna, M. Salih, P. Dean, A. G. Davies, and E. H. Linfield, "Electrically tunable terahertz quantum-cascade laser with a heterogeneous active region," Appl. Phys. Lett. **95**, 181101 (2009).
[49]P. Dean, M. Salih, S. P. Khanna, L. H. Li, N. K. Saat, A. Valavanis, A. Burnett, J. E. Cunningham, A. G. Davies, and E. H. Linfield, "Resonant-phonon depopulation terahertz quantum cascade lasers and their application in spectroscopic imaging," Semicond. Sci. Technol. **27**, 094004 (2012).
[50]K. K. Choi, B. F. Levine, R. J. Malik, J. Walker, and C. G. Bethea, "Periodic negative conductance by sequential resonant tunneling through an expanding high-field superlattice domain," Phys. Rev. B **35**, 4172–4175 (1987).
[51]T. H. H. Vuong, D. C. Tsui, and W. T. Tsang, Appl. Phys. Lett. **52**, 981 (1988); J. Appl. Phys. **66**, 3688 (1989).
[52]H. T. Grahn, H. Schneider, and K. v. Klitzing, "Optical detection of high-field domains in GaAs/AlAs superlattices," Appl. Phys. Lett. **54**, 1757–1759 (1989).
[53]H. T. Grahn, R. J. Haug, W. Muller, and K. Ploog, "Electric-field domains in semiconductor superlattices: A novel S stem for tunneling between 2D Systems," Phys. Rev. Lett. **67**, 1618–1621 (1991).
[54]H. T. Grahn, H. Schneider, and K. v. Klitzing, Phys. Rev. B **41**, 2890 (1990).
[55]M. Wienold, L. Schrottke, M. Giehler, R. Hey, and H. T. Grahn, "Nonlinear transport in quantum-cascade lasers: The role of electric-field domain formation for the laser characteristics," J. Appl. Phys. **109**, 073112 (2011).
[56]D. Ban, E. H. Sargent, St. J. Dixon-Warren, I. Calder, A. J. SpringThorpe, R. Dworschak, G. Este, and J. K. White, "Direct imaging of the depletion region of an InP pn junction under bias using scanning voltage microscopy," Appl. Phys. Lett. **81**, 5057–5059 (2002).
[57]D. Ban, E. H. Sargent, St. J. Dixon-Warren, K. Hinzer, I. Calder, A. J. SpringThorpe, and J. K. White, "Scanning voltage microscopy on active semiconductor lasers: The impact of doping profile near an epitaxial growth interface on series resistance," IEEE J. Quantum Electron. **40**, 651–655 (2004).